Front. Chem. Sci. Eng. 2025, 19(4): 31
https://doi.org/10.1007/s11705-025-2532-7

RESEARCH ARTICLE

Predictive neural network model and empirical equations for the physico–chemical properties and solvent characteristics of potassium carbonate solutions in carbon capture processes

Abolhasan Ameri (✉)

Department of Chemical Engineering, KTH Royal Institute of Technology, Stockholm SE-10044, Sweden

Abstract Controlling and optimizing carbon capture processes is vital for improving efficiency, reducing energy consumption, and enhancing sustainability. Process analytical technology (PAT) plays a crucial role in achieving these goals. Establishing the relationship between physico–chemical properties (PCPs) and solvent characteristics, such as loading and strength, can facilitate the practical implementation of PAT. This study develops empirical models for the PCPs of potassium carbonate solutions, including density, refractive index, and electrical conductivity, as well as a mechanistic model for pH across varying temperatures, solvent concentration, and solvent loadings. The models showed strong agreement with experimental data. Density and refractive index increased with solvent strength and decreased with temperature, while conductivity correlated with solvent strength and temperature but decreased with solvent loading. A feed-forward neural network was trained to predict solvent strength and loading using eight input scenarios. The highest accuracy was achieved with PCPs combined with Fourier transform infrared (FTIR) or ultraviolet-visible (UV-Vis), using only PCPs, or using PCPs with FTIR and UV-Vis while excluding pH. The findings provide essential insights into K_2CO_3 solution behavior, contributing to advances in carbon capture technologies.

Keywords potassium carbonate solution, empirical equations, feed-forward neural network model, physico–chemical properties, solvent strength and loading

Received September 23, 2024; accepted December 15, 2024;
online March 7, 2025

E-mail: aboame@kth.se

1 Introduction

CO_2 emissions from fossil fuels are harmful to the environment, contributing significantly to global climate change [1]. The Paris Agreement, established in 2015, underscores the urgent need to address this issue by committing to limit global warming to below 2 °C. To achieve this goal, it is essential to reduce CO_2 emissions from fossil fuels, as they are a major driver of climate change. By cutting these emissions, we can work toward a more sustainable future and meet the targets set by the Paris Agreement [2].

To achieve meaningful reductions in CO_2 emissions, the integration of carbon capture, utilization, and storage (CCUS) technologies is becoming increasingly vital [3,4]. CCUS offers a practical solution by capturing CO_2 at its source, such as fossil fuel power plants, and either repurposing it for industrial uses or permanently storing it underground to prevent it from entering the atmosphere [5,6]. This technology plays a key role in mitigating the environmental impact of continued fossil fuel use, allowing for a transitional pathway toward a low-carbon economy while ensuring that emissions targets are met [7]. In addition to CCUS technologies, bioenergy with carbon capture and storage (BECCS) presents another promising approach for reducing CO_2 emissions [8]. BECCS involves using biomass, a renewable energy source, to generate energy while capturing and storing the CO_2 produced during the process [9]. Since biomass absorbs CO_2 during its growth, BECCS can achieve negative emissions, effectively removing more CO_2 from the atmosphere than it emits [10]. When combined with CCUS, BECCS offers a powerful strategy to not only curb emissions from fossil fuels but also to actively reduce atmospheric CO_2 levels.

One effective method for implementing CCUS or BECCS is the absorption process within a post-combustion strategy [11,12]. In this approach, CO_2 is captured from the flue gases produced after the combustion of fossil fuels or biomass. The absorption method typically involves the use of chemical solvents which selectively capture CO_2 from the gas mixture. When described in greater detail, this process typically includes the following steps [13]. Initially, the flue gas, which consists of CO_2 along with other gases like nitrogen and water vapor, is cooled to an optimal temperature (T) between 40 and 60 °C to enhance the efficiency of the absorption process [14]. The cooled flue gas is then directed through an absorption column or scrubber, where it interacts with a liquid solvent, often an amine-based solution such as monoethanolamine, or alternatives like K_2CO_3 or NaOH solutions. The solvent selectively reacts with the CO_2 in the flue gas, creating a CO_2-rich solvent mixture. The CO_2-rich solvent is then pumped to a regeneration unit, usually a stripper, where it is heated to the T of between 100 and 140 °C to break the chemical bond between the CO_2 and the solvent [15]. This releases the CO_2 in a concentrated form, which can then be compressed and transported for storage or utilization. The regenerated solvent, now free of CO_2, is cooled and recycled back to the absorption column to capture more CO_2 from incoming flue gas [16].

The regeneration section in carbon capture and storage (CCS) plants is a critical component, but it is also the most energy-intensive and costly part of the carbon capture process [17,18]. The heating during regeneration requires significant energy input, often sourced from the plant's own power generation, which reduces the overall efficiency of the facility [19,20]. Additionally, the high energy demand for solvent regeneration contributes substantially to the operational costs of CCS plants. Consequently, improving the energy efficiency of the regeneration process is a key area of research, as it holds the potential to lower both the economic and environmental costs of carbon capture technologies [21].

Managing solvent loading (θ) in the CCS process is an effective way to control energy consumption in the regeneration section [22]. θ refers to the amount of CO_2 absorbed by the solvent relative to its capacity [23]. If the solvent is under-loaded (absorbing less CO_2 than it can), more solvent must be circulated to capture the same amount of CO_2, leading to higher energy use in both the absorption and regeneration stages. On the other hand, if the solvent is over-loaded (saturated with CO_2), it may require more energy to release the CO_2 during regeneration, as the chemical bonds between the CO_2 and the solvent become stronger and harder to break. Therefore, maintaining an effective θ, where the solvent captures an efficient amount of CO_2 without becoming overly saturated, can reduce the volume of solvent that needs to be processed in the regeneration section. This reduces the energy required for heating the solvent, leading to lower overall energy consumption and cost in the CCS process. Adjusting θ is thus a crucial strategy for improving the energy efficiency of carbon capture systems.

One of the common methods for measuring θ in carbon capture processes is liquid titration [24,25]. This technique involves determining the concentration of CO_2 in the solvent by reacting the solution with a titrant and measuring the amount required to complete the reaction. While widely used, liquid titration has several disadvantages. It is a time-consuming process, often requiring multiple steps to obtain accurate results. Additionally, it demands significant manual labor, as the procedure involves careful handling of chemicals and equipment. Furthermore, titration can be prone to human error, leading to potential inaccuracies in the measurements [26]. Due to these limitations, more efficient and automated methods for monitoring θ are often sought in CCS applications.

Process analytical technology (PAT) is an advanced approach used to monitor and control the θ in CCS plants, ensuring that the process operates efficiently. PAT involves the use of real-time analytical tools and sensors to continuously measure key process parameters, such as the concentration of CO_2 in both the flue gas and the solvent, along with the physico–chemical properties (PCPs) of the CO_2-rich solvent exiting the bottom of the absorber column [27]. This real-time data enables dynamic adjustments to the process conditions, such as flow rates and T values, to maintain effective θ. For example, if PAT sensors detect that the solvent is approaching overloading, the system can be adjusted to reduce the CO_2 concentration in the solvent, thus preventing excessive energy consumption during regeneration. By providing continuous, accurate insights into the process, PAT helps to maintain the balance between effective CO_2 capture and efficient energy use. This real-time control ensures that the K_2CO_3 solvent operates efficiently, thus improving the overall CO_2 capture process. This not only enhances the performance of the CCS plant but also reduces operational costs by minimizing unnecessary energy expenditure. Additionally, the use of PAT can improve the overall reliability and stability of the CCS process, leading to more consistent and sustainable carbon capture operations.

K_2CO_3 solution is a commonly used solvent in CCS processes [28]. When K_2CO_3 absorbs CO_2 from flue gas, it transforms into $KHCO_3$ [29]. Consequently, the outlet of the absorber features a mixture of K_2CO_3, $KHCO_3$, and H_2O in the rich solvent flow. The varying concentrations of these salts in the mixture correspond to different values of solvent strength (X) and θ [30]. In our previous research, we measured the PCPs of these solutions, including density (ρ), refractive index (RI), electrical conductivity (κ), and pH, in addition to Fourier transform infrared (FTIR) and ultraviolet-visible (UV-Vis) spectroscopy data at various θ, molar concentrations (m), and T [30]. This study introduces a mechanistic model to predict pH and three empirical models for predicting ρ, RI, and κ of K_2CO_3 solution. The pH and κ are influenced by X, θ, and T, whereas ρ and RI depend only on X and T. Additionally, we propose a feed-forward neural network (FFNN) model, based on experimental data from our prior study, to predict X and θ of the K_2CO_3 solution using different properties as input data.

According to the literature, some studies have proposed models for predicting the PCPs of electrolyte solutions. Li et al. [31] introduced a model for estimating the density of both single and mixed electrolyte solutions. Their approach treated the solution as a mixture of ionic hard spheres and compressible water under the influence of external pressure. However, their study did not include K_2CO_3 or $KHCO_3$ solutions. Building on their previous work, Li and Lee [32] further developed their model, but once again, their results did not include K_2CO_3 or $KHCO_3$ solutions. Laliberté and Cooper [33] developed an empirical model for calculating the density of 59 aqueous electrolyte solutions, including K_2CO_3. The model's parameters were m and T. Additionally, they explored the possibility of applying this model to systems containing two electrolytes dissolved in water. Lam et al. [34] proposed a method for calculating the density of both single and multiple saline solutions. Their study covered 17 aqueous solutions containing two, three, or four salts, with the method focusing on the anions and cations present in these solutions. K_2CO_3 was included as one of the single salts examined in their research.

Tang and Munkelwitz [35] devised a computational approach to determine the RI of electrolyte systems, including $(NH_4)_2SO_4 \cdot H_2O$, $Na_2SO_4 \cdot H_2O$, and $NaNO_3 \cdot H_2O$, across a broad range of m values. Leyendekkers and Hunter [36,37] attempted to develop a model to predict the RI of various electrolyte solutions across different T values, pressures, and wavelengths. They evaluated 15 different solvents in their study; however, K_2CO_3 or $KHCO_3$ were not among the solvents tested. Alavia et al. [38] reported on the modeling of the RI for binary aqueous solutions of various compounds, including boric acid, sodium chloride, potassium chloride, sodium sulfate, lithium sulfate, and potassium sulfate. Farooque et al. [39] developed a straightforward model to predict the RI of six different solutions, including three electrolyte solutions: KCl, NaCl, and $CaCl_2$. Their model was dependent on both m and T.

Bernard et al. [40] investigated the conductance of ionic solutions using equilibrium pair correlation. Their modeling results showed good agreement with experimental data for NaCl, KBr, $BaCl_2$, and $LaCl_3$. de Diego et al. [41] proposed an empirical model for the electrolytic conductivity of concentrated electrolyte solutions, which was dependent on both m and T. Their model was an extension of the Casteel-Amis equation. In a subsequent study, they refined their earlier model based on the Falkenhagen equation to address aqueous electrolyte solutions at very high m values. To account for deviations from ideality at elevated m values, they incorporated the concept of activity into the model [42]. Chandra and Bagchi [43] developed a theoretical model for the conductance of electrolyte solutions, using a mode coupling theory approach to account for electrolyte friction. Wang et al. [44] developed a comprehensive model for calculating the electrical conductivity of aqueous or mixed-solvent electrolytes across a wide range of m values. Their model included a correlation for determining ionic conductivities at infinite dilution. Ding [45] utilized the empirical Casteel-Amis equation to fit experimental data on the conductivity of electrolytes as a function of salt concentration. Ding et al. [46] introduced a fitting equation based on the Casteel-Amis equation to model conductivity as a function of m and T. This equation was applied to super-concentrated aqueous electrolytes. Bernard and Aupiais [47] predicted the electrical conductivity of certain weak electrolytes, taking into account additional interactions, such as chemical associations involved in acid-base equilibria, beyond the typical hard-sphere interactions at short distances and Coulombic interactions at longer distances. Zhang et al. [48] proposed a semi-empirical equation with five parameters, which is based on the number of free ions and ion mobility as functions of m and T. This equation is designed for solutions at medium and high m values. Boroujeni et al. [49] compared the electrical conductivity of electrolyte solutions using six different models: the Debye-Hückel-Onsager limiting law, the extended law, the smaller ion shell model, as well as the full mean spherical approximation (MSA) and the simplified MSA models, and the Quint-Viallard model.

In this study, we aim to address a critical gap in the literature by developing a predictive model for the PCPs of K_2CO_3 and $KHCO_3$ solutions, including pH, ρ, RI, and κ, and how they relate to X, θ, and T. The novelty of our work lies in the integration of a FFNN model with these properties and spectral data (FTIR and UV-Vis) to predict θ and X. This approach allows for real-time monitoring and control of the CO_2 capture process, particularly in the solvent regeneration stage, where energy consumption is a key challenge. By employing this novel predictive model, we significantly enhance the process efficiency, providing an innovative solution that could reduce operational costs and improve the sustainability of carbon capture technologies. The application of the FFNN model in this context offers a more efficient and automated alternative to traditional methods, highlighting the practical implications and significance of this study in advancing CCUS technologies.

2 Models

This section presents empirical models for predicting the ρ, RI, and κ of a solution containing K_2CO_3, $KHCO_3$, and H_2O, as well as a mechanistic model for calculating the pH of the solution. Additionally, a FFNN was implemented for prediction of θ and strength using those PCPs database. The modeling platform utilized in this study was MATLAB. The database was established based on experimental data collected from our previous study [30], focusing on the properties of solutions containing K_2CO_3, $KHCO_3$, and H_2O measured at various T, X, and θ. Here, θ is defined as the ratio of moles of CO_2 absorbed to moles of native K_2CO_3 in the solution (Eq. (1)):

$$\theta = \frac{\text{Moles CO}_2\text{ absorbed}}{\text{Moles K}_2\text{CO}_3\text{ equivalents}}. \tag{1}$$

X is defined as the weight percentage (wt%) of K_2CO_3 equivalents in the primary solution, when no CO_2 is absorbed, and it contains only K_2CO_3 and water (Eq. (2)):

$$X = \text{wt\% K}_2\text{CO}_3\text{ equivalents}. \tag{2}$$

When no CO_2 absorption occurs, the loading is zero. As CO_2 absorption increases, K_2CO_3 reacts with CO_2, forming more $KHCO_3$, which leads to a gradual reduction of K_2CO_3 and an increase in $KHCO_3$. This corresponds to an increase in the θ value, eventually reaching a loading of 1 when all K_2CO_3 has been converted to $KHCO_3$. The experimental data covered a T range of 293.2 to 353.2 K, X from 5 to 30 wt%, and θ from 0 to 1. It should be noted that X ranging from 5 to 30 wt% correspond to m between 0.378 and 2.818 $\text{mol}\cdot\text{L}^{-1}$. In the empirical equations developed for ρ, RI, and κ, as well as in the mechanistic model for pH, the parameter m is used as an independent variable instead of X.

The empirical models were developed using nonlinear regression analysis techniques. They were derived by fitting experimental data collected at various T, m, and θ. The functional form of the equations includes multiple terms involving powers, logarithmic, and exponential functions of the independent variables, T and m, to capture their effects on the ρ, RI, and κ of the solution. The constants (P_1 to P_9) in the equation of ρ and κ, and P_1 to P_{10} for RI were obtained using nonlinear regression techniques, where MATLAB was employed to minimize the difference between the predicted and experimental values through an optimization algorithm. The accuracy of the model was validated using statistical parameters such as the coefficient of determination (R^2) and the absolute average relative error percentage (AARD%), confirming its reliability in predicting the ρ across the studied range of conditions.

It should be noted that the terms included in the empirical formulas have been thoroughly evaluated for significance and that any redundant or insignificant terms have been excluded to maintain the integrity of the model. A summary diagram is provided in Fig. 1 to enhance understanding of the concepts discussed in the following sections.

2.1 Empirical equation for density

As the experimental data indicate, ρ values depend only on T and m, but not on θ. Therefore, the proposed empirical equation is solely based on these two parameters:

$$\rho = \rho_{H_2O} + \exp\Bigg(P_1 + P_2 \times m^{0.5} \times \ln m + P_3 \times (\ln m)^2 \times P_4 \times m^{0.5} + \frac{P_5}{m^{0.5}} + \frac{P_6}{T^{1.5}} + P_7 \times \frac{\ln T}{T^2} + \frac{P_8}{T^2} + P_9 \times \exp(-T)\Bigg), \tag{3}$$

where ρ and ρ_{H_2O} represent the densities ($\text{kg}\cdot\text{m}^{-3}$) of the

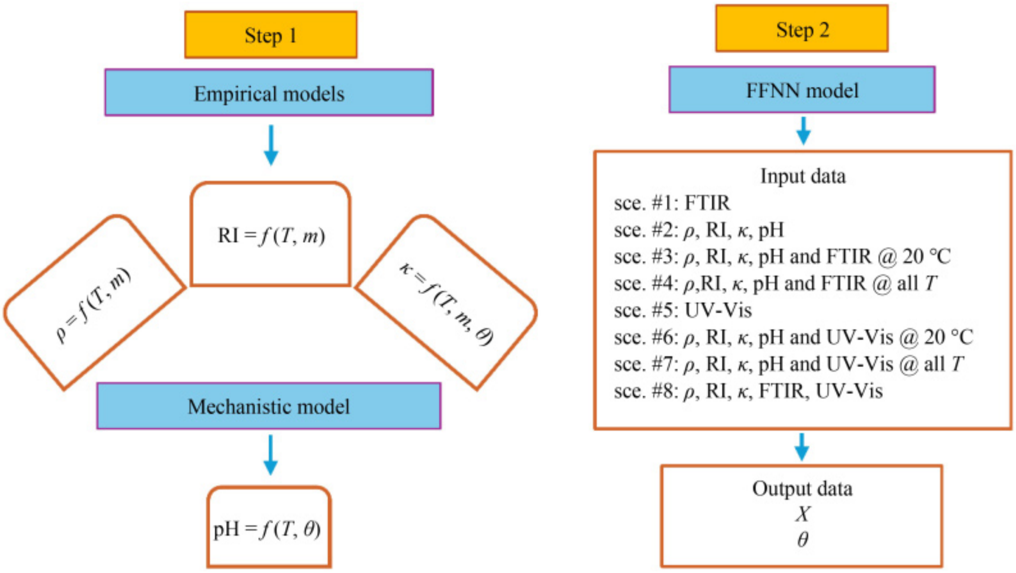

Fig. 1 Summary diagram of the models in this study.

solution and water, respectively; T is the temperature (°C); m is the molar concentration ($\mathrm{mol \cdot L^{-1}}$); P_1 to P_9 are specific constants to this empirical equation. And $\rho_{\mathrm{H_2O}}$ can be calculated using the Kell Equation [50]:

$$\rho_{\mathrm{H_2O}} = \frac{\left(\left(\left(\left(-2.805 \times 10^{-10} \times T + 1.055 \times 10^{-7}\right) T - 4.617 \times 10^{-5}\right) T - 0.00798\right) T + 16.945\right) T + 999.8352}{1 + 0.01687T}. \tag{4}$$

To assess the precision of the model, the R^2 and AARD% were calculated.

2.2 Empirical equation for RI

For RI, a similar approach to that used for ρ is applied, as it depends only on T and m, and not on θ. The empirical equation proposed for the RI of K_2CO_3 solution, based on the experimental data, is as follows:

$$\begin{aligned}\mathrm{RI} = {} & \mathrm{RI}_{\mathrm{H_2O}} + P_1 + P_2 m + P_3 \ln T + P_4 m^2 + P_5 (\ln T)^2 + \\ & P_6 m \ln T + P_7 m^3 + P_8 (\ln T)^3 + P_9 m (\ln T)^2 + P_{10} m^2 \ln T,\end{aligned} \tag{5}$$

where $\mathrm{RI}_{\mathrm{H_2O}}$ represents the RI of water, while m is the molar concentration ($\mathrm{mol \cdot L^{-1}}$). P_1 to P_{10} are constants specific to the equation. The accuracy of the model was evaluated by calculating the R^2 and AARD%. $\mathrm{RI}_{\mathrm{H_2O}}$ is calculated using the Lorentz-Lorentz function of liquid water [51]:

$$\mathrm{RI}_{\mathrm{H_2O}} = \sqrt{\frac{2xx + 1}{1 - xx}}, \tag{6}$$

where xx is calculated as follows:

$$\begin{aligned} xx = \rho^* \times \Bigg(& a_0 + a_1 \times \rho^* + a_2 \times T^* + a_3 \times (\lambda^*)^2 \times T^* + \frac{a_4}{(\lambda^*)^2} + \\ & \frac{a_5}{(\lambda^*)^2 - (\lambda^*_{\mathrm{UV}})^2} + \frac{a_6}{(\lambda^*)^2 - (\lambda^*_{\mathrm{IR}})^2} + a_7 \times (\rho^*)^2 \Bigg), \end{aligned} \tag{7}$$

$$\rho^* = \frac{\rho}{\rho_0}, \ \rho_0 = 1000\ \mathrm{kg \cdot m^{-3}},$$

$$\lambda^* = \frac{\lambda}{\lambda_0}, \ \lambda_0 = 0.589\ \mathrm{\mu m},$$

$$T^* = \frac{T}{T_0}, \ T_0 = 273.15\ \mathrm{K}, \tag{8}$$

where λ is the wavelength and T is the absolute temperature; a_0 to a_7, along with λ^*_{UV} and λ^*_{IR}, are coefficients, which are provided in Table 1.

2.3 Empirical equation for electrical conductivity

Unlike ρ and RI, κ depends on all three parameters: T, m, and θ. Therefore, the proposed empirical equation includes T and m, with distinct coefficients P_1 to P_9 derived and reported for each θ value. The proposed equation for the prediction of κ is as follows:

$$\kappa = \frac{P_1 + P_2 m + P_3 m^2 + P_4 m^3 + P_5 \ln T}{1 + P_6 m + P_7 m^2 + P_8 m^3 + P_9 \ln T}, \tag{9}$$

where κ is the electrical conductivity ($\mathrm{mS \cdot cm^{-1}}$). The model's precision was assessed by determining R^2 and AARD% parameters.

2.4 Mechanistic model for pH

The pH model, which mathematically relates pH to m and θ, is derived from a system of five reactions and balances. The first step involves utilizing the reaction rate equations for the three primary reactions that occur during CO_2 absorption in a K_2CO_3 solution:

$$CO_2 + H_2O \overset{k_1}{\leftrightarrow} HCO_3^- + H^+, \ k_1 = \frac{[HCO_3^-][H^+]}{[CO_2]} \tag{10}$$

$$HCO_3^- \overset{k_2}{\leftrightarrow} CO_3^{2-} + H^+, \ k_2 = \frac{\left[CO_3^{2-}\right][H^+]}{[HCO_3^-]} \tag{11}$$

$$H_2O \overset{k_w}{\leftrightarrow} H^+ + OH^-, \ k_w = [OH^-][H^+] \tag{12}$$

where k_1, k_2, and k_w are the reaction rate constants for each reaction. Here, k_w refers to the auto-protolysis of water, and the relations for k_1 and k_2 are taken from Danckwerts [52]. These constants are T-dependent and are given by the following equations:

$$\log_{10} k_1 = \frac{-3404.7}{T} + 14.843 - 0.03279T, \tag{13}$$

$$\log_{10} k_2 = \frac{-2902.4}{T} + 6.498 - 0.0238T. \tag{14}$$

Additionally, the charge and carbon balances are

Table 1 Coefficients of Eq. (7)

Parameter	Value
a_0	0.243905091
a_1	$9.53518094 \times 10^{-3}$
a_2	$-3.64358110 \times 10^{-3}$
a_3	$2.65666426 \times 10^{-4}$
a_4	$1.59189325 \times 10^{-3}$
a_5	$2.45733798 \times 10^{-3}$
a_6	0.897478251
a_7	$-1.63066183 \times 10^{-2}$
λ^*_{UV}	0.2292020
λ^*_{IR}	5.432937

included:

$$2m + [\mathrm{H}^+] = 2\left[\mathrm{CO}_3^{2-}\right] + [\mathrm{HCO}_3^-] + [\mathrm{OH}^-], \quad (15)$$

$$m(1+\theta) = \left[\mathrm{CO}_3^{2-}\right] + [\mathrm{HCO}_3^-] + [\mathrm{CO}_2]. \quad (16)$$

By rewriting Eq. (15) to solve for [H$^+$] and substituting all other concentrations in this equation with Eqs. (10)–(12), which are expressed as functions of [H$^+$], an equation for [H$^+$] as a function of m and θ can be derived. The pH is then calculated using the following relationship:

$$\mathrm{pH} = -\log_{10}[\mathrm{H}^+]. \quad (17)$$

The final mathematical model for pH is expressed as follows:

$$[\mathrm{H}^+]^4 + [\mathrm{H}^+]^3(k_1 + 2m) + [\mathrm{H}^+]^2(k_1k_2 + mk_1(1-\theta) - k_w) - [\mathrm{H}^+](k_1k_w + 2mk_1k_2\theta) - k_1k_2k_w = 0. \quad (18)$$

2.5 FFNN model for prediction of solvent loading and strength

In this study, we employ a FFNN to predict the variables X and θ based on initial input data. The FFNN is a type of artificial neural network where connections between nodes do not form a cycle, and it operates in a layered architecture: input layer, one or more hidden layers, and an output layer. This architecture enables the network to learn complex patterns and relationships within the data, making it well-suited for our prediction tasks.

2.5.1 Architecture

The FFNN used in this study consists of the following components.

2.5.1.1 Input layer

The input layer receives the initial data, which includes the features required to make predictions about X and θ. Each feature corresponds to an input node in this layer. The input data used for training the model comprised six different properties, including four PCPs (i.e., ρ, RI, κ, and pH), as well as FTIR and UV-Vis spectra all of which are taken from our previous study [30]. These properties were measured over a T range of 20–80 °C, with X values between 5 and 30 wt% and θ values ranging from 0.0 to 1.0.

Eight different scenarios were considered based on combinations of these properties. In the first scenario, only FTIR spectra were used as input data. The second scenario included only the four PCPs. The third scenario combined PCPs and FTIR data measured at 20 °C. Since the FTIR and UV-Vis instruments were only capable of measuring spectra at 20 °C, data for other T values were unavailable. Consequently, one of the scenarios involved using only PCP data at 20 °C along with the FTIR spectra. In another scenario, to account for PCP data across all T (20–80 °C), the FTIR spectra from 20 °C were duplicated for samples with the same X and θ characteristics but at higher T values. Thus, the fourth scenario included PCPs and FTIR data for all T values. In the fifth scenario, only UV-Vis spectra were used as input data. In the sixth case, PCPs combined with UV-Vis spectra measured only at 20 °C were considered. In the following scenario, the UV-Vis spectra from 20 °C were duplicated for samples with the same X and θ at higher T, so both PCP and UV-Vis data across all T values were included. Lastly, in the eighth scenario, the input data consisted of FTIR, UV-Vis spectra, and PCPs excluding pH. Table 2 provides a summary of these scenarios.

The rationale behind selecting different scenarios was to evaluate the model's robustness and accuracy under various conditions. In real-world applications, sensor failures may occur, resulting in the unavailability of one or more data sources. Testing the model with different inputs allows us to assess its sensitivity and determine which scenario yields the most precise predictions of X and θ.

2.5.1.2 Hidden layers

The network includes two hidden layers, each consisting of a specified number of neurons. These layers are responsible for learning and extracting features from the input data through nonlinear transformations. The activation function used in the hidden layers is the Rectified Linear Unit, which introduces nonlinearity into the model and helps in learning complex patterns.

To determine the optimal number of hidden layers and neurons for the FFNN, we conducted a model complexity analysis by testing various architectures. The architectures tested included different combinations of hidden layer sizes and neuron counts, specifically: a single hidden layer with 10, 20, and 30 neurons [10], [20], [30]; two hidden layers with combinations of neurons: [10,5], [20,10], [30,20].

These configurations were evaluated using 5-fold cross-validation to assess model performance. The performance of each architecture was measured by calculating the mean squared error (MSE) on the validation sets. Based on the results, the model with the lowest validation MSE

Table 2 Various input data scenarios used for training the model

Scenario number	Input data
1	FTIR
2	PCP
3	PCP and FTIR (T = 20 °C)
4	PCP and FTIR (various T)
5	UV-Vis
6	PCP and UV-Vis (T = 20 °C)
7	PCP and UV-Vis (various T)
8	FTIR, UV-Vis, and PCP without pH

was selected as the most optimized architecture for predicting the desired outcomes. Increasing the number of hidden layers did not enhance the model's accuracy, and therefore, additional layers were not included in the complexity evaluation analysis. This analysis allowed us to fine-tune the neural network structure and ensure a balance between model complexity and prediction accuracy.

2.5.1.3 Output layer

The output layer consists of two neurons, one for each target variable: X and θ. The final output is computed using a linear activation function to ensure that the predictions can take on a wide range of values, as required for regression tasks. Figure 2 illustrates the schematic of the FFNN topology.

2.5.2 Training process

The FFNN is trained using backpropagation with a MSE loss function. Training was performed using the Levenberg-Marquardt algorithm with specified parameters. The training process involves the following steps.

2.5.2.1 Normalization and standardization of input data

Normalization and standardization are essential preprocessing techniques in data analysis and machine learning. These methods are used to adjust the scales of features or variables before feeding them into models. Normalization scales the data to a fixed range, typically between 0 and 1. This ensures that all features have the same scale, regardless of their original range.

$$X_{\text{norm.}} = \frac{X - X_{\min}}{X_{\max} - X_{\min}}. \tag{19}$$

where $X_{\min}$ and $X_{\max}$ are the minimum and maximum values of the feature X in the dataset, respectively.

Standardization transforms the data to have a mean of zero and a standard deviation of one. This technique assumes that the data follows a Gaussian distribution and ensures that all features are on the same scale in terms of their variance.

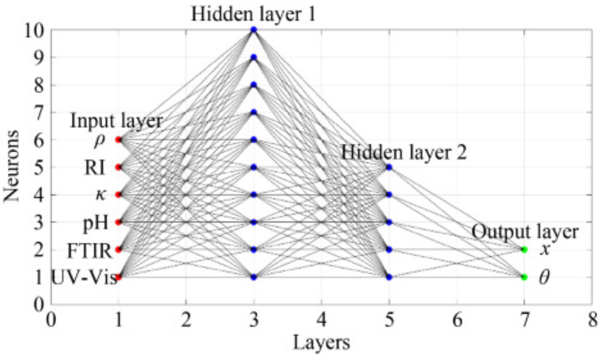

Fig. 2 A schematic of the FFNN topology.

$$X_{\text{std.}} = \frac{X - \mu}{\sigma}, \tag{20}$$

where μ and σ represent the mean and standard deviation of the feature, respectively.

2.5.2.2 Training set size

To determine the optimal training size, a model size analysis was performed. Various training set sizes, including 50%, 60%, 70%, 80%, and 90% of the total data points, were tested, with the remaining data serving as the prediction set for each configuration. The MSE values for each set were then compared to identify the most appropriate training set size.

2.5.2.3 Forward propagation

During forward propagation, the input data are passed through the network, layer by layer, to compute the predicted values of X and θ. Each neuron's output is calculated based on the weighted sum of inputs and the activation function applied.

2.5.2.4 Loss calculation

The difference between the predicted values and the actual values (ground truth) is computed using the MSE loss function. This loss quantifies the error in the predictions and guides the optimization process.

2.5.2.5 Backpropagation

Backpropagation involves calculating the gradient of the loss function with respect to each weight in the network. The gradients are used to update the weights through optimization algorithms such as stochastic gradient descent or Adam, which iteratively adjust the weights to minimize the loss.

2.5.2.6 Epochs and batch size

The network is trained over 100 epochs, where each epoch consists of passing the entire training data set through the network. Additionally, a batch size is used to determine the number of samples processed before updating the weights, which helps in stabilizing the training process. The batch size is implicitly set to the total number of training examples.

2.5.3 Statistical analysis

2.5.3.1 Predicted values analysis

After training the model and predicting X and θ values for each scenario, these predictions were compared to the experimental values of X and θ. Additionally, these predicted values were used to calculate the PCPs using the empirical models for ρ, RI, and κ, along with the mechanistic model for pH described earlier in sections 2.1 to 2.4. These results were then compared with the experimental data from our previous study [30]. To evaluate the accuracy of the trained model and empirical equations, the R^2 was employed in all comparisons. R^2 is a straightforward statistical metric that indicates how well a model fits the observed data. It essentially serves as a measure of the model's effectiveness. Typically, the closer the R^2 value is to 1, the more accurately the model reflects the data.

2.5.3.2 Model's robustness analysis

Robustness analysis is used for FFNN models to ensure that the model performs consistently well across various scenarios and conditions. It helps identify how sensitive the model is to changes in inputs, parameters, or data distributions. By evaluating robustness, we can assess the model's stability, reliability, and generalization capabilities, ensuring that it maintains accurate predictions even when faced with slight variations or uncertainties in the data.

In this study, we employed leave-one-out cross validation (LOOCV) to evaluate the robustness of our neural network model. LOOCV is a rigorous method used to assess the generalizability of a model by systematically excluding each data point from the training set and then testing the model's performance on this excluded data point. The data set, which includes various input features and output variables, was divided into training and test sets in a sequential manner. Each iteration of LOOCV involves one data point being left out of the training process while the remaining data points are used to train the model. For each iteration, a neural network model was trained on the training set, which comprises all data points except the one left out. The model's performance was then evaluated on the excluded data point. This process was repeated for each data point in the data set, resulting in a total of as many models as there are data points. After training the model on each subset, predictions were made for the excluded data point. The predictions for all data points were aggregated to analyze the overall performance of the model. The average predictions across all iterations were calculated for both output variables. Additionally, the standard deviation of these predictions was computed to quantify the variability and reliability of the model. Standard errors of the mean were derived from these standard deviations to create error bars for visualization. The predicted values from the LOOCV were compared against experimental data to assess the model's accuracy. R^2 values were computed to measure the goodness of fit, providing insight into how well the model predictions match the experimental observations. To visualize the model's performance, parity plots were created. These plots compare the predicted values against the experimental data, with error bars representing the standard errors. Additionally, normalized values were plotted to evaluate the model's predictions across different data subsets.

Another method applied to assess the robustness of our neural network model was a k-fold cross-validation approach. This technique helps evaluate the model's performance and generalizability by partitioning the data set into multiple subsets or "folds". 5-fold and 10-fold cross-validation strategies were chosen. This means that the data set was divided into 5 and 10 equal-sized folds. In each iteration of the cross-validation process, 1 fold was used as the test set, and the remaining 4- and 9-folds were used as the training set. This procedure was repeated 5 and 10 times, with each fold serving as the test set once. For each fold, the neural network model was trained using the training subset. After training, predictions were made on the entire data set. The average predictions for θ and X across all folds were calculated. This step involved normalizing the predictions by subtracting the mean of predictions from each fold and dividing by the mean. This normalization process was performed separately for each column of predictions. To visualize the performance and variability across different folds, plots were generated showing normalized values of θ and X against fold numbers. The plots display how predictions vary from fold to fold, providing insights into the model's performance consistency. Lines connecting the data points in the plots highlight trends and fluctuations in predictions across the folds.

3 Results and discussion

This section presents the results of the constants of proposed models for four key PCPs, namely ρ, RI, κ, and pH, evaluated at various values of T, m, and θ. The model predictions are compared with experimental data to assess their accuracy. Additionally, a comparison is made between different scenarios of the FFNN model for predicting X and θ, and the corresponding calculations of PCPs based on these predictions, in order to determine which scenario provides the best predictive performance.

3.1 Density

The constants for the empirical equation for ρ, as presented in Eq. (3), are reported in Table 3 along with the R^2 and AARD% values for the model's performance.

Figure 3 illustrates the comparison between experimental data and the results generated by the proposed empirical model. As shown in Fig. 3(a), the experimental and modeled data align closely, indicating good agreement. The density of a solution is influenced by both m and T due to their impact on molecular interactions and spacing. As the X increases, the concentration of dissolved solutes rises. This increases the number of particles in a given volume, leading to more mass per unit volume, which results in a higher ρ. The solvent molecules are more tightly packed because of increased intermolecular forces, reducing free space and raising the overall ρ. When the T rises, the kinetic energy of the molecules increases. This causes the molecules to move more rapidly and occupy more space. The increased thermal motion reduces intermolecular forces, causing the solution to expand and its ρ to decrease, as the same mass now occupies a larger volume. In the parity plot shown in Fig. 3(b), which compares experimental ρ data with model predictions, the data points are closely aligned along the diagonal line. This alignment indicates a high level of agreement between the experimental values and the model's predictions, demonstrating that the model accurately captures the density relationships. Overall, the plot confirms the model's reliability in predicting ρ values within the tested range. In Fig. 3(c), the residual plot is presented, which further validates the model's reliability. The residual plot displays the differences between the observed experimental values and the model's predicted values. A patternless distribution of residuals around zero, with no systematic trends, indicates that the model is accurately capturing the underlying data without significant biases. This suggests that the model performs well across the entire range of data, reinforcing the credibility of its predictions.

Table 3 Constants for the empirical ρ equation in Eq. (3)

Parameter	Value
P_1	–0.6847
P_2	–0.47228
P_3	0.422076
P_4	0.668201
P_5	–2.19093
P_6	1.671058
P_7	1.477266
P_8	1.171182
P_9	–9.00776
R^2	0.9997
AARD%	0.0977

3.2 RI

The empirical equation for the RI is detailed in Eq. (5). The constants used in this model, along with R^2 and AARD%, are presented in Table 4.

Figures 4(a)–4(c) mirror the validation approach used in Fig. 3. Specifically, Fig. 4(a) shows the comparison between experimental RI data and model predictions, indicating a strong agreement between the two data sets. Figure 4(b) presents a parity plot, where the experimental versus modeled RI values closely follow the diagonal line, reflecting accurate predictions by the model. Figure 4(c) features the residual plot, which reveals that

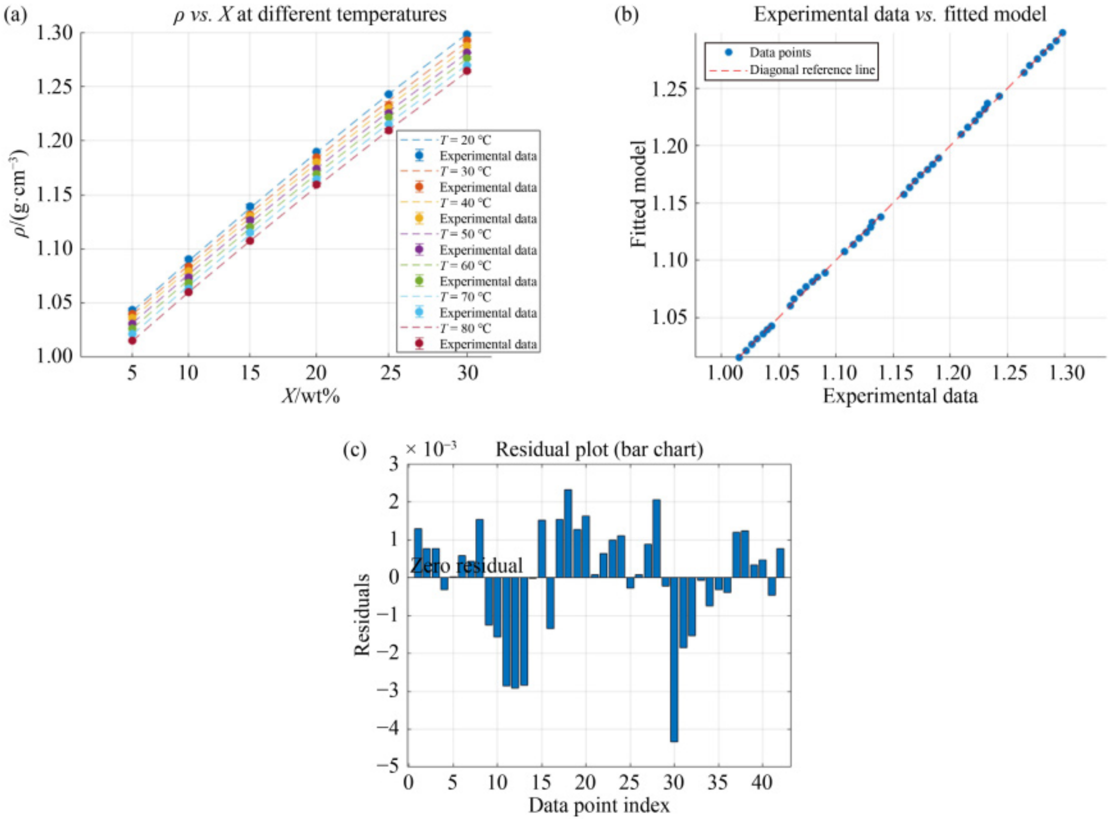

Fig. 3 Model validation and comparison for ρ: (a) comparison of experimental ρ data with predictions from the empirical model, (b) parity plot, and (c) residual plot.

the residuals are evenly distributed around zero without any systematic pattern, further confirming the model's reliability. The analysis of the RI reveals distinct trends with varying conditions. As shown in the results, RI increases with X at a constant T, indicating that higher m lead to a higher RI. This can be attributed to the increased ρ of the solvent mixture, which typically enhances the interaction between light and the medium, resulting in a higher RI. Conversely, RI decreases with T at a constant X. This behavior is consistent with the general principle that most substances have a lower RI at higher T due to thermal expansion, which reduces the ρ and alters the light's interaction with the medium. Additionally, similar to ρ, the RI does not exhibit any significant dependency on the variable θ, indicating that θ does not substantially influence RI in the context of this empirical model as was observed in the experimental data.

Table 4 Constants for the empirical RI equation in Eq. (5)

Parameter	Value
P_1	0.034523
P_2	0.044959
P_3	–0.0171
P_4	–0.00228
P_5	0.000978
P_6	–0.0113
P_7	0.000176
P_8	0.000294
P_9	0.00131
P_{10}	7.89E–06
R^2	0.9994
AARD%	0.0189

3.3 Electrical conductivity

The coefficients for the empirical equation of κ, as defined in Eq. (9), are listed in Table 5. These coefficients, denoted as P_1 to P_9, vary with different values of θ, ranging from 0 to 1.0, and are accompanied by the corresponding R^2 and AARD% values for each case.

Figure 5 illustrates the comparison between experimental and modeled conductivity data for each θ value. It includes a series of figures, similar to Fig. 4(a), which depict the experimental data versus model predictions, and a series of parity plots, similar to Fig. 4(b), which validate the model's accuracy.

As X increases, also increases κ when T and θ are held constant. This trend can be attributed to the fact that higher X typically enhances the ionization of the solute, leading to more charged particles in the solution and, consequently, higher conductivity. κ increases with T at constant X and θ. Elevated T values generally enhance the mobility of ions in the solution, thereby increasing conductivity. This is due to the reduced viscosity of the solvent at higher T values, which facilitates easier

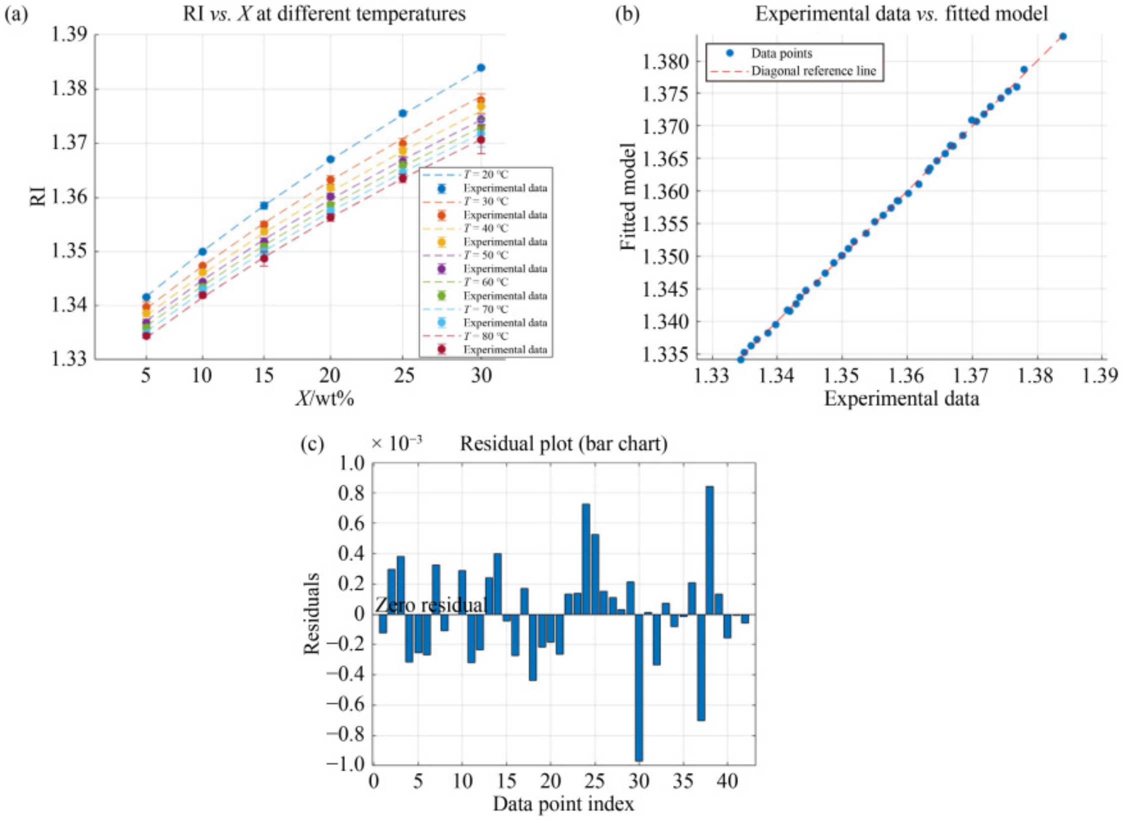

Fig. 4 Model validation and comparison for RI: (a) comparison of experimental RI data with predictions from the empirical model, (b) parity plot, and (c) residual plot.

Table 5 Constants for the empirical κ equation in Eq. (9)

Parameter	$\theta = 0.0$	$\theta = 0.1$	$\theta = 0.2$	$\theta = 0.3$	$\theta = 0.4$	$\theta = 0.5$	$\theta = 0.6$	$\theta = 0.7$	$\theta = 0.8$	$\theta = 0.9$	$\theta = 1.0$
P_1	7.0820	1.7090	7.7810	3.3192	–6.9055	–4.0834	–4.2014	0.5712	1.2466	1.6955	0.3002
P_2	45.8551	56.1653	46.6695	51.4198	63.7630	57.4330	61.3491	53.1916	54.9033	55.0664	58.6833
P_3	2.3906	–5.8980	–1.0262	–3.6688	–12.9307	–9.6389	–14.6691	–7.4422	–10.2380	–11.2013	–15.6083
P_4	–2.4724	–0.7325	–1.5561	–1.2335	0.5329	0.0307	1.2276	–0.5254	0.3958	0.6605	1.9131
P_5	–0.2501	0.5589	–0.4690	0.4578	2.6177	2.2924	2.0793	1.0770	0.7450	0.5227	0.7110
P_6	–0.0429	0.0042	–0.0322	–0.0191	0.0050	–0.0196	–0.0122	–0.0173	–0.0096	–0.0098	–0.0139
P_7	0.0458	0.0073	0.0319	0.0239	–0.0016	0.0148	0.0045	0.0193	0.0113	0.0107	0.0079
P_8	–0.0104	–0.0023	–0.0069	–0.0058	–0.0002	–0.0030	–0.0003	–0.0047	–0.0022	–0.0020	–0.0004
P_9	–0.1893	–0.1900	–0.1886	–0.1875	–0.1840	–0.1830	–0.1833	–0.1864	–0.1874	–0.1881	–0.1867
R^2	0.9999	0.9998	0.9998	0.9998	0.9995	0.9997	0.9997	0.9998	0.9999	0.9998	0.9998
AARD%	0.4786	0.7071	0.8045	0.7879	0.8214	0.7738	0.7950	0.7564	0.6909	0.6845	0.7362

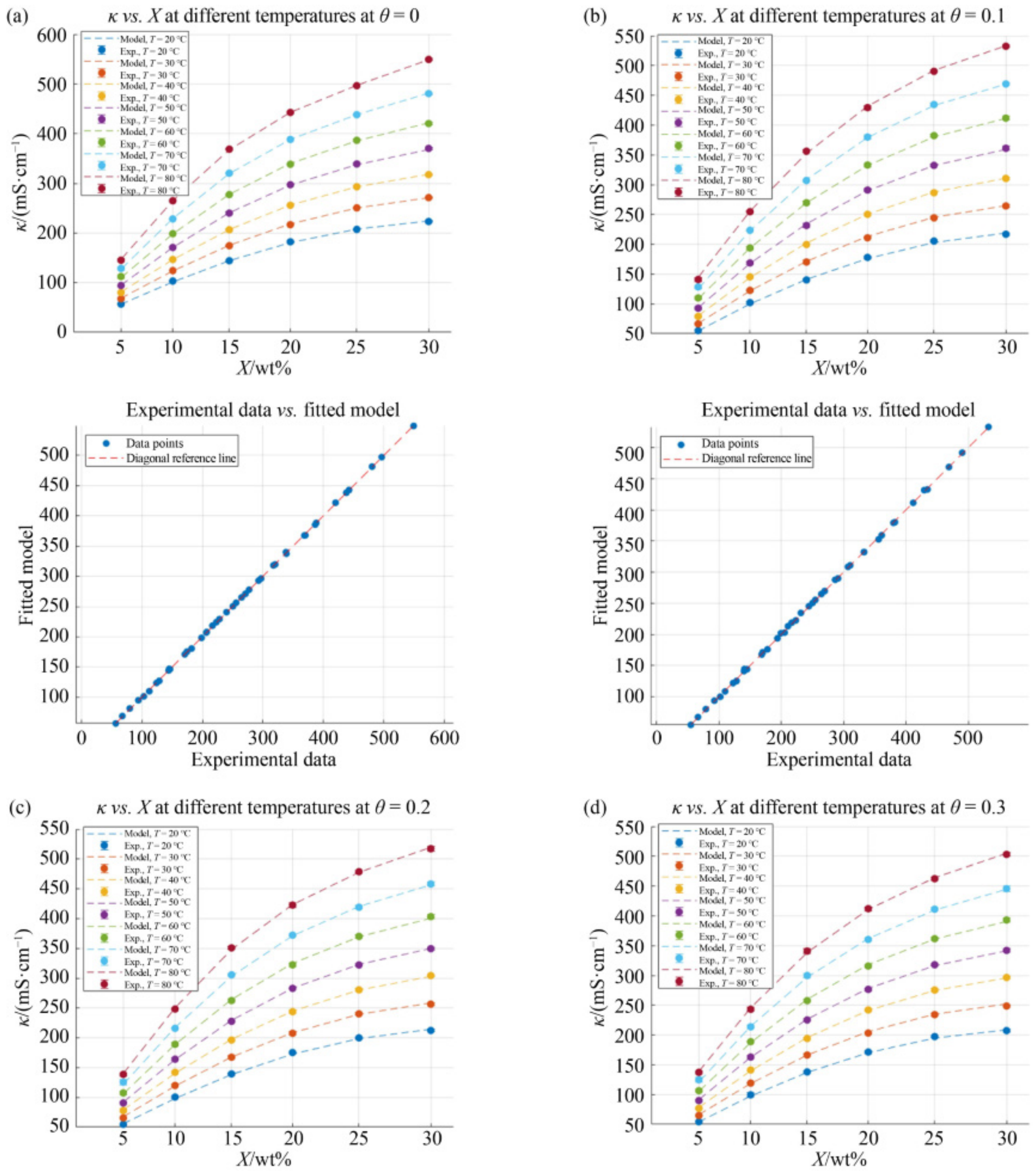

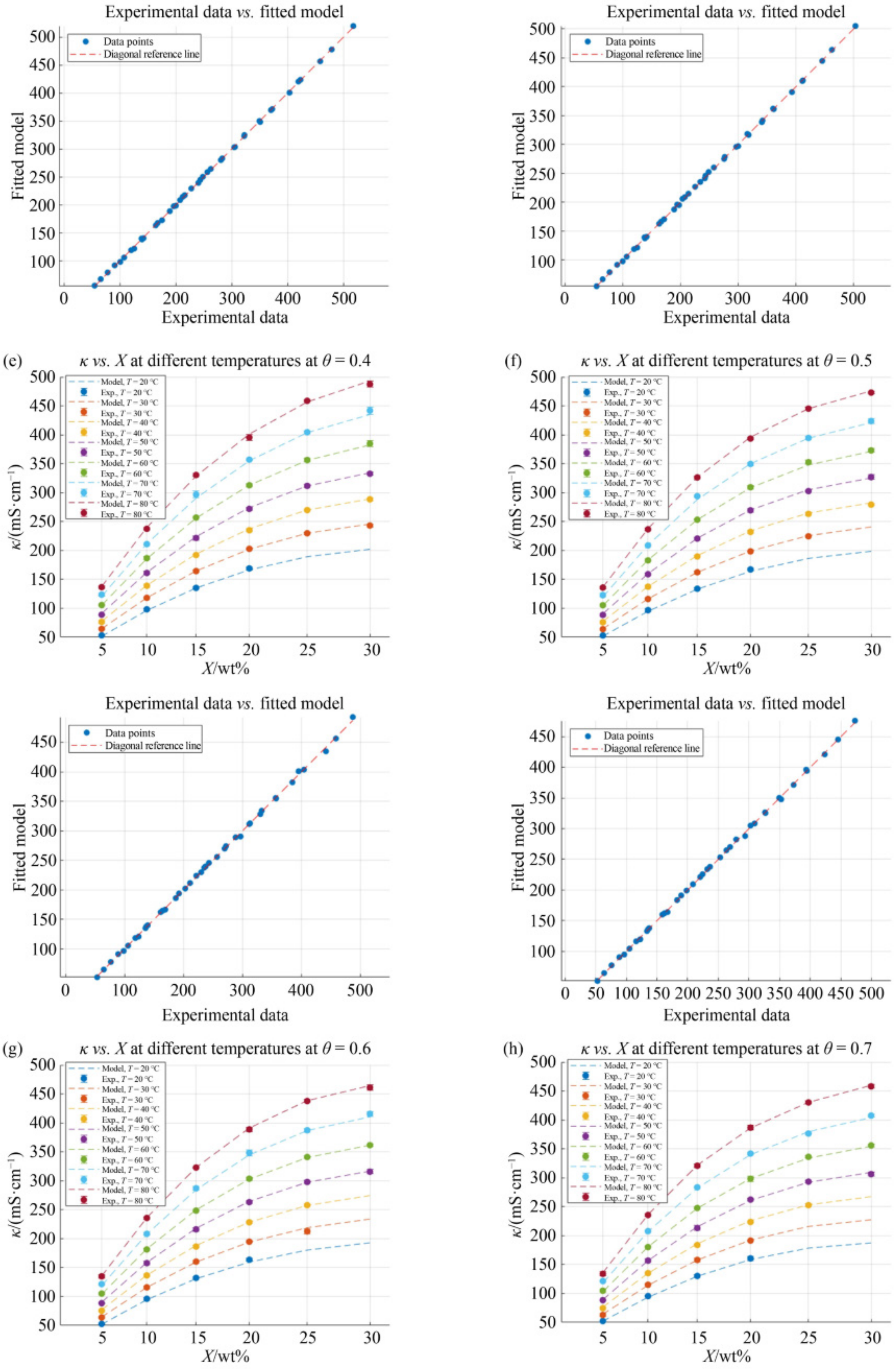
Experimental data *vs.* fitted model
Data points
Diagonal reference line
Fitted model
Experimental data
0
100
200
300
400
500
100
150
200
250
300
350
400
450
500
Experimental data *vs.* fitted model
Data points
Diagonal reference line
Fitted model
Experimental data
(e)
κ *vs.* X at different temperatures at $\theta = 0.4$
Model, T = 20 °C
Exp., T = 20 °C
Model, T = 30 °C
Exp., T = 30 °C
Model, T = 40 °C
Exp., T = 40 °C
Model, T = 50 °C
Exp., T = 50 °C
Model, T = 60 °C
Exp., T = 60 °C
Model, T = 70 °C
Exp., T = 70 °C
Model, T = 80 °C
Exp., T = 80 °C
κ/(mS·cm^{-1})
X/wt%
5
10
15
20
25
30
50
(f)
κ *vs.* X at different temperatures at $\theta = 0.5$
κ/(mS·cm^{-1})
X/wt%
Experimental data *vs.* fitted model
Data points
Diagonal reference line
Fitted model
Experimental data
Experimental data *vs.* fitted model
Data points
Diagonal reference line
Fitted model
Experimental data
(g)
κ *vs.* X at different temperatures at $\theta = 0.6$
κ/(mS·cm^{-1})
X/wt%
(h)
κ *vs.* X at different temperatures at $\theta = 0.7$
κ/(mS·cm^{-1})
X/wt%

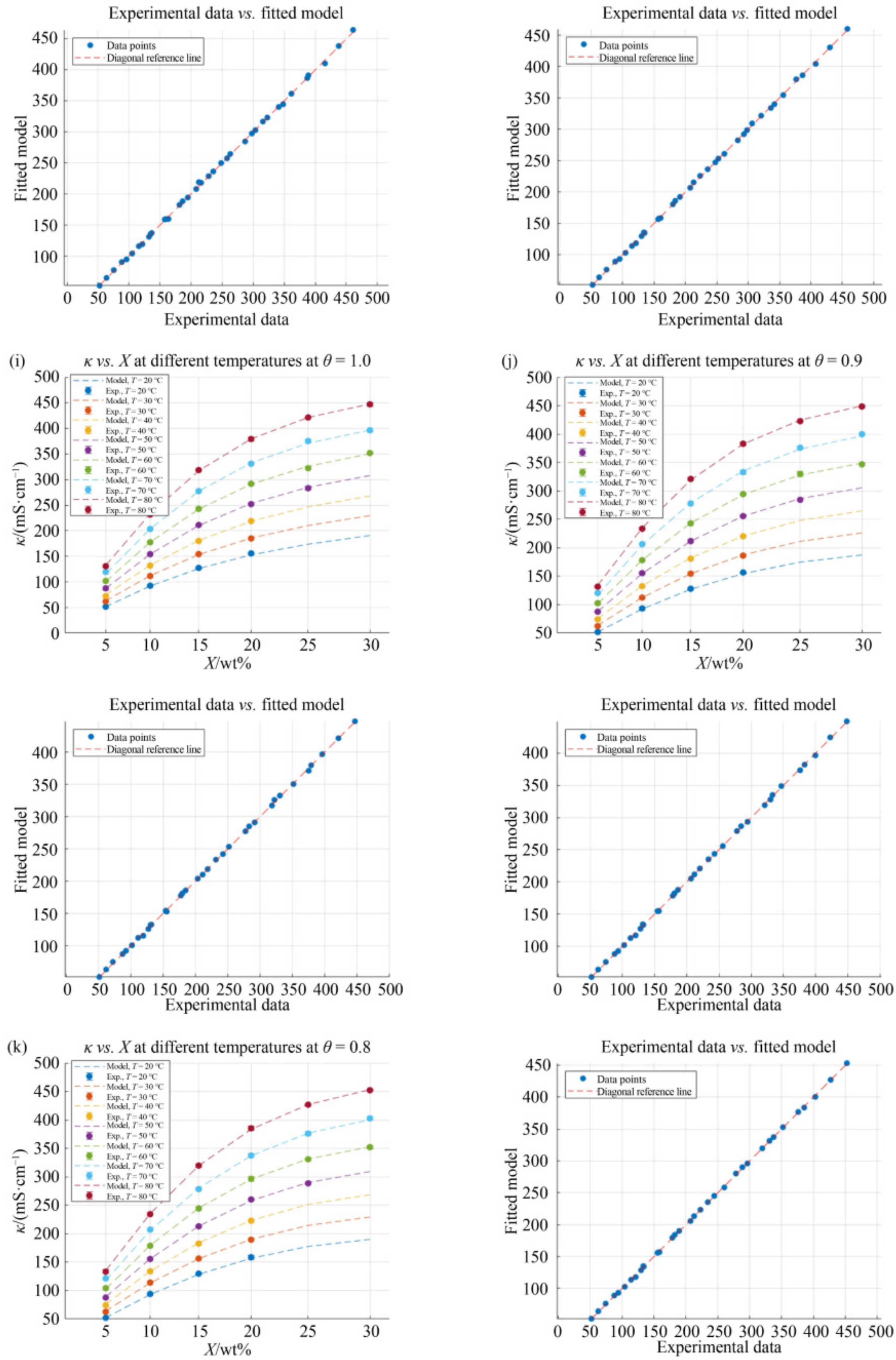

Fig. 5 Model validation and comparison for κ for (a) $\theta = 0$, (b) $\theta = 0.1$, (c) $\theta = 0.2$, (d) $\theta = 0.3$, (e) $\theta = 0.4$, (f) $\theta = 0.5$, (g) $\theta = 0.6$, (h) $\theta = 0.7$, (i) $\theta = 0.8$, (j) $\theta = 0.9$, and (k) $\theta = 1.0$.

movement of charged particles. An increase in θ results in a decrease in conductivity while keeping X and T constant. This inverse relationship suggests that as θ increases, the solute's ability to conduct electricity diminishes. Increasing θ from 0 to 1 results in a higher proportion of $KHCO_3$ and a lower proportion of K_2CO_3. This shift reduces the concentration of highly mobile carbonate ions in favor of less mobile bicarbonate ions, leading to a decrease in conductivity. This effect is due to the inherent differences in ion mobilities, where carbonate ions, having a higher mobility, contribute more effectively to conductivity compared to bicarbonate ions.

The results show a good match between experimental data and model predictions, as evidenced by the parity plots and comparison figures. The empirical model effectively captures the dependencies of conductivity on X, T, and θ.

3.4 pH

Figure 6 consists of six subplots, each representing a constant X value and showing the variations of pH with

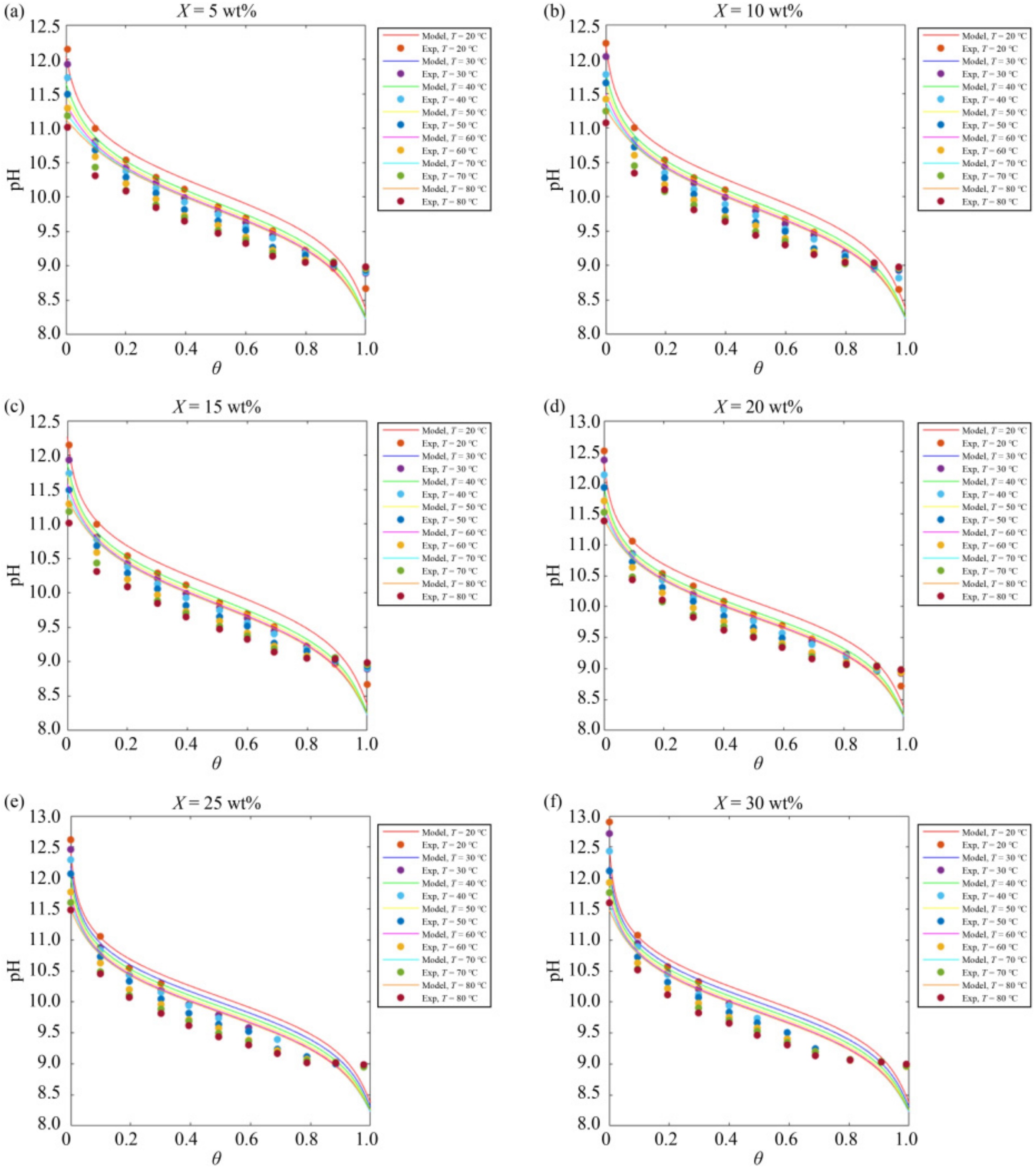

Fig. 6 The variation of pH with θ and T at six different constant X: (a) X = 5 wt%, (b) X = 10 wt%, (c) X = 15 wt%, (d) X = 20 wt%, (e) X = 25 wt%, and (f) X = 30 wt%.

T and *θ*. As *θ* increases, the pH decreases, and similarly, an increase in *T* also results in a lower pH. The reasoning behind this behavior has been comprehensively explained in our previous study [30]. Regarding the effect of *X* on pH, aside from low solvent loadings (θ = 0.0 and 0.1), the pH remains relatively stable across different *m* values at constant *T* for intermediate to high *θ* values. However, at low loadings, an increase in *X* leads to a rise in pH.

As shown, there are some discrepancies between the experimental data and the modeling results for pH. Since the model is mechanistic, it has certain limitations. One notable issue is the assumption of an ideal solution, which introduces errors. Additionally, the reaction rate constants k_1, k_2, and k_w, used for the three primary reactions occurring in the absorption process, are based on dilute solutions. To improve the model's accuracy, it would be beneficial to update these rate constats by calculating the reaction kinetics for real, non-ideal solutions.

3.5 FFNN model for prediction of *X* and *θ*

The parity plots for *X* and *θ*, predicted using the trained FFNN model based on the eight different scenarios outlined in Table 2, are displayed in Fig. 7. Generally, the *X* predictions are more accurate and closer to the experimental data compared to the *θ* predictions. Using FTIR or UV-Vis spectra alone as input data, as in

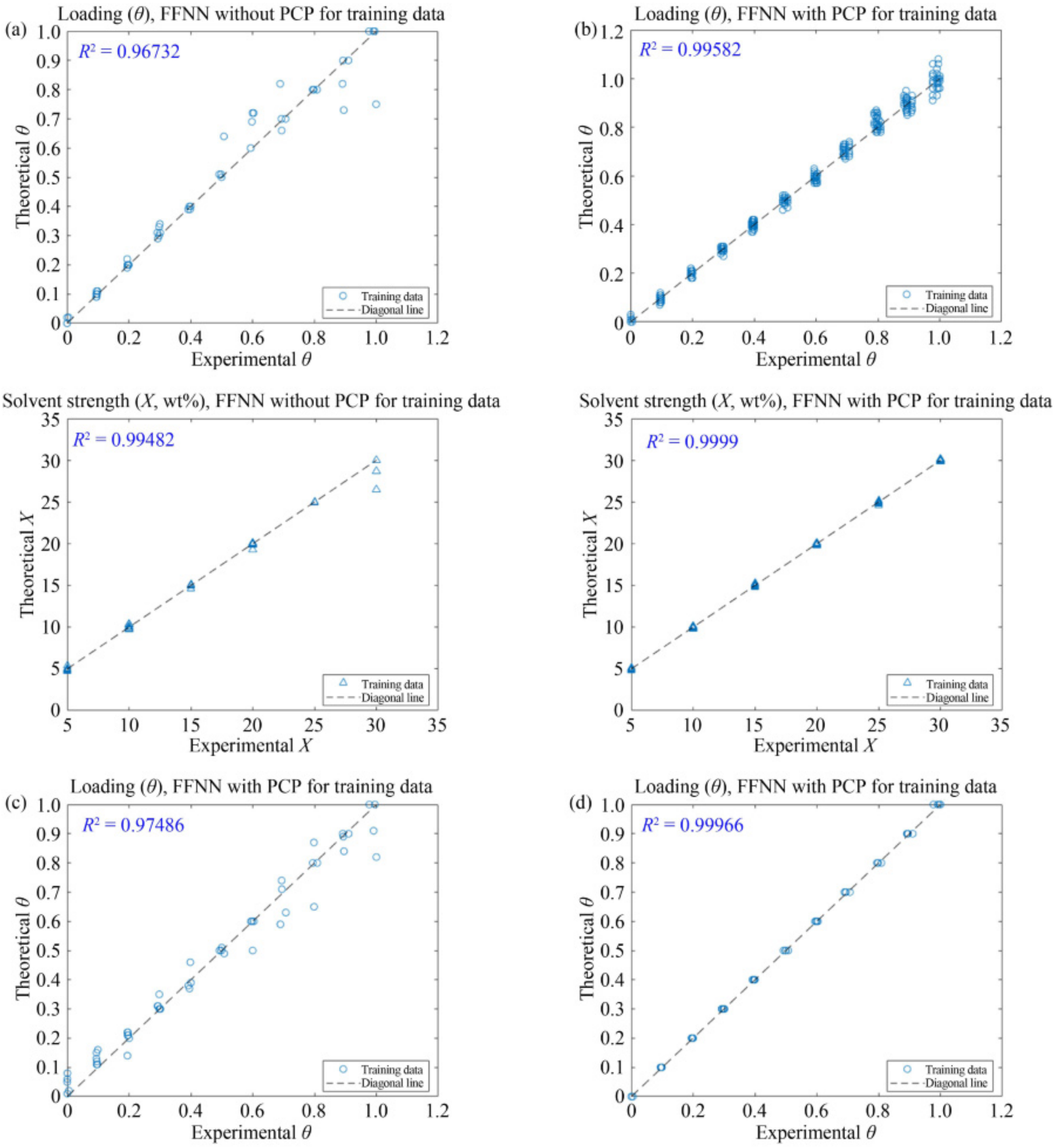

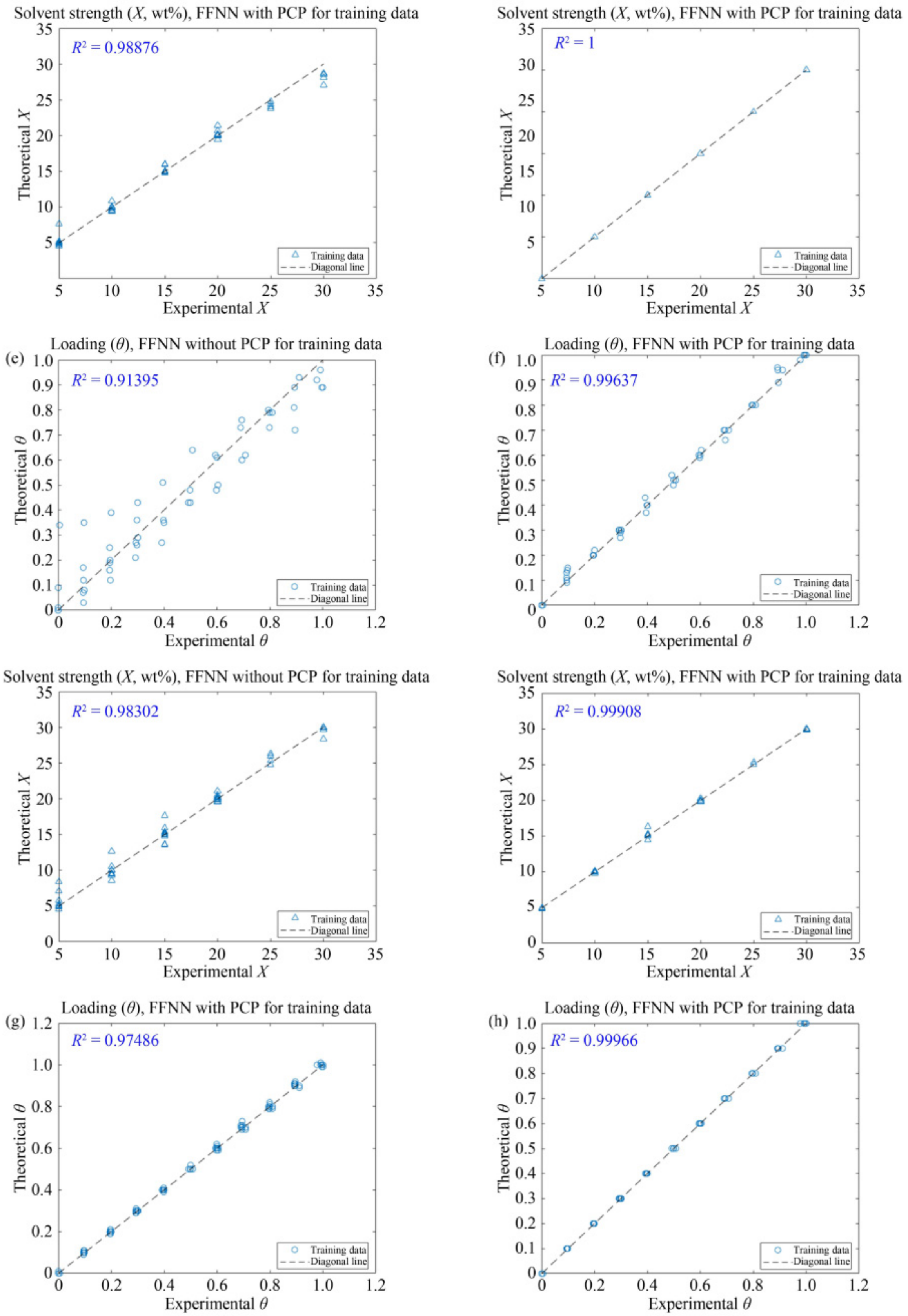
Solvent strength (X, wt%), FFNN with PCP for training data
$R^2 = 0.98876$
Theoretical X
Experimental X
Training data
Diagonal line
Solvent strength (X, wt%), FFNN with PCP for training data
$R^2 = 1$
Theoretical X
Experimental X
Training data
Diagonal line
(e)
Loading (θ), FFNN without PCP for training data
$R^2 = 0.91395$
Theoretical θ
Experimental θ
Training data
Diagonal line
(f)
Loading (θ), FFNN with PCP for training data
$R^2 = 0.99637$
Theoretical θ
Experimental θ
Training data
Diagonal line
Solvent strength (X, wt%), FFNN without PCP for training data
$R^2 = 0.98302$
Theoretical X
Experimental X
Training data
Diagonal line
Solvent strength (X, wt%), FFNN with PCP for training data
$R^2 = 0.99908$
Theoretical X
Experimental X
Training data
Diagonal line
(g)
Loading (θ), FFNN with PCP for training data
$R^2 = 0.97486$
Theoretical θ
Experimental θ
Training data
Diagonal line
(h)
Loading (θ), FFNN with PCP for training data
$R^2 = 0.99966$
Theoretical θ
Experimental θ
Training data
Diagonal line

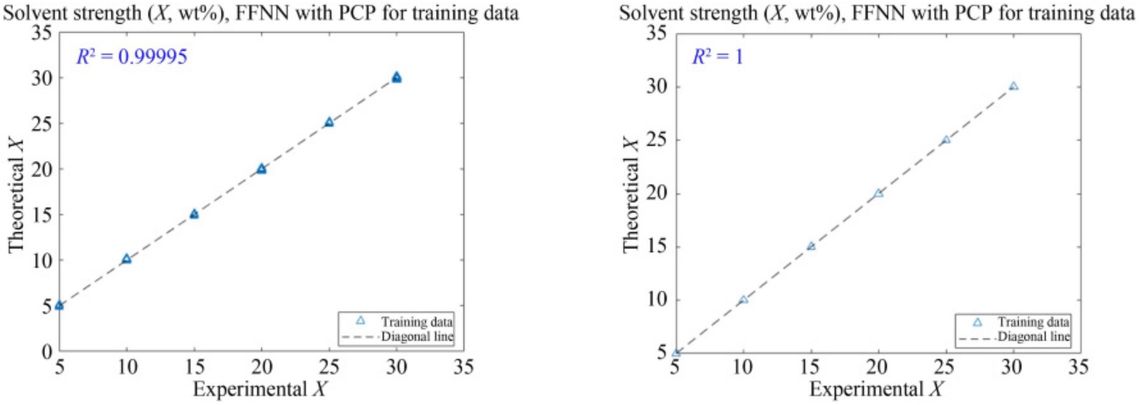

Fig. 7 Parity plots comparing X and θ predictions from the trained FFNN model across eight different input scenarios: (a) FTIR, (b) PCP, (c) PCP and FTIR at $T = 20$ °C, (d) PCP and FTIR at various T values, (e) UV-Vis, (f) PCP and UV-Vis at $T = 20$ °C, (g) PCP and UV-Vis at various T values, and (h) FTIR, UV-Vis, and PCP excluding pH.

scenarios 1 and 5, results in poor predictions for both θ and X. The R^2 values are 0.96732 for θ and 0.99482 for X in scenario 1, and 0.91395 for θ and 0.98302 for X in scenario 5, indicating that these properties alone are insufficient as inputs for the FFNN model.

In scenarios 3 and 6, where PCP data are combined with FTIR or UV-Vis at $T = 20$ °C, the model still fails to predict X and θ accurately. Scenario 3 yields R^2 values of 0.97486 for θ and 0.98876 for X, while scenario 6 shows values of 0.99637 for θ and 0.99908 for X. This is due to the exclusion of high-T data points, limiting the model's accuracy. Scenario 2, which uses only PCP data as input, provides acceptable predictions for both X and θ, with R^2 values exceeding 0.99 for both variables (0.99582 for θ and 0.99990 for X).

The most accurate predictions are found in scenarios 4 and 7, where PCP data are combined with FTIR or UV-Vis at all T values. In scenario 4, R^2 values of 0.99966 for θ and 1.00000 for X were obtained, while scenario 7 resulted in R^2 values of 0.99940 for θ and 0.99995 for X. This highlights that incorporating all PCP data along with FTIR or UV-Vis at all T range leads to the highest precision in predicting θ and X.

In scenario 8, where FTIR, UV-Vis, and PCP (excluding pH) were used as input, similar high precision was achieved, with R^2 values of 0.99966 for θ and 1.00000 for X. This indicates that even when one PCP cannot be measured during the process, FTIR and UV-Vis can compensate and still provide accurate predictions. For visual comparison, the R^2 values for θ and X across all scenarios are presented in Fig. 8, highlighting the varying prediction accuracy of different input combinations.

3.5.1 Calculation of PCPs from predicted X and θ (from FFNN model) using the proposed equations

For these eight scenarios, after predicting X and θ, these values were then used to calculate the PCPs using the

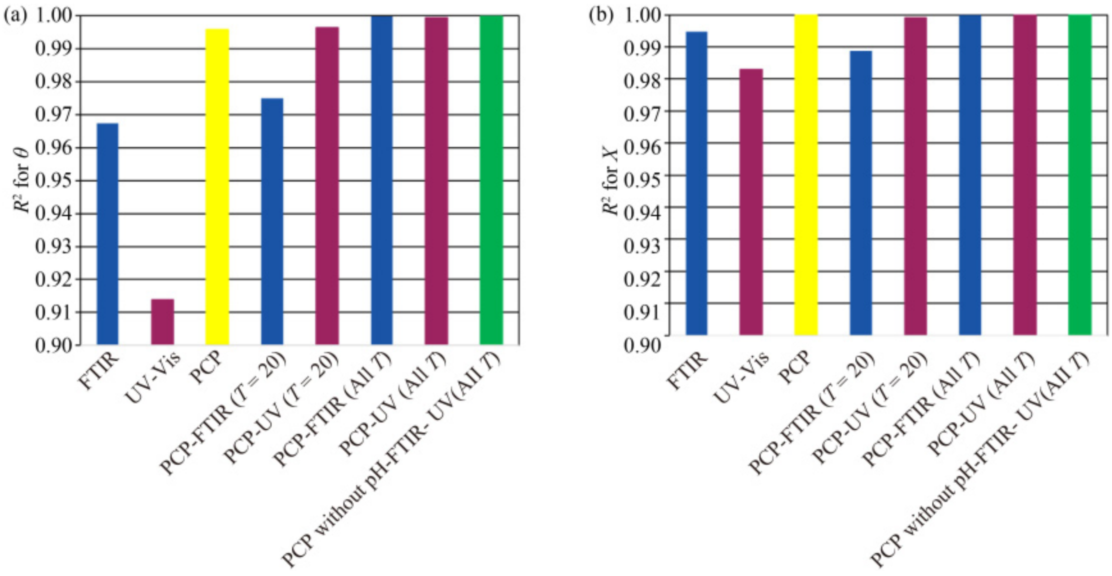

Fig. 8 Visual comparison of the R^2 values for (a) θ and (b) X across all eight scenarios, illustrating the differences in prediction accuracy based on various input combinations used in the FFNN model.

empirical and mechanistic equations proposed in this study. The parity plots in Fig. 9 display a similar trend to those in Fig. 7, indicating that when X and θ are accurately predicted, the calculated PCPs also exhibit high precision such as in scenarios 2, 4, 7, and 8. However, in cases where the predictions of X and θ were less accurate such as in scenarios 1, 3, 5, and 6, applying the empirical equations for ρ, RI, and κ, along with the mechanistic model for pH, led to lower R^2 values and greater discrepancies in the parity plots.

3.5.2 Model's size analysis

Various training set sizes were tested for the FFNN model, and the corresponding MSE values were compared. The lowest MSE was observed when 80% of the total data was used for training (MSE = 0.00020251). Therefore, all scenarios were trained using this 80% training data configuration. Figure 10(a) illustrates the MSE values for different training set sizes.

3.5.3 Model's complexity analysis

Figure 10(b) illustrates the MSE values for various model architectures, examining the effect of different numbers of hidden layers and neurons per layer. The architecture [10, 5], consisting of two hidden layers with 10 and 5 neurons, achieved the lowest MSE value of 0.0004. Consequently, this architecture was used for training all models.

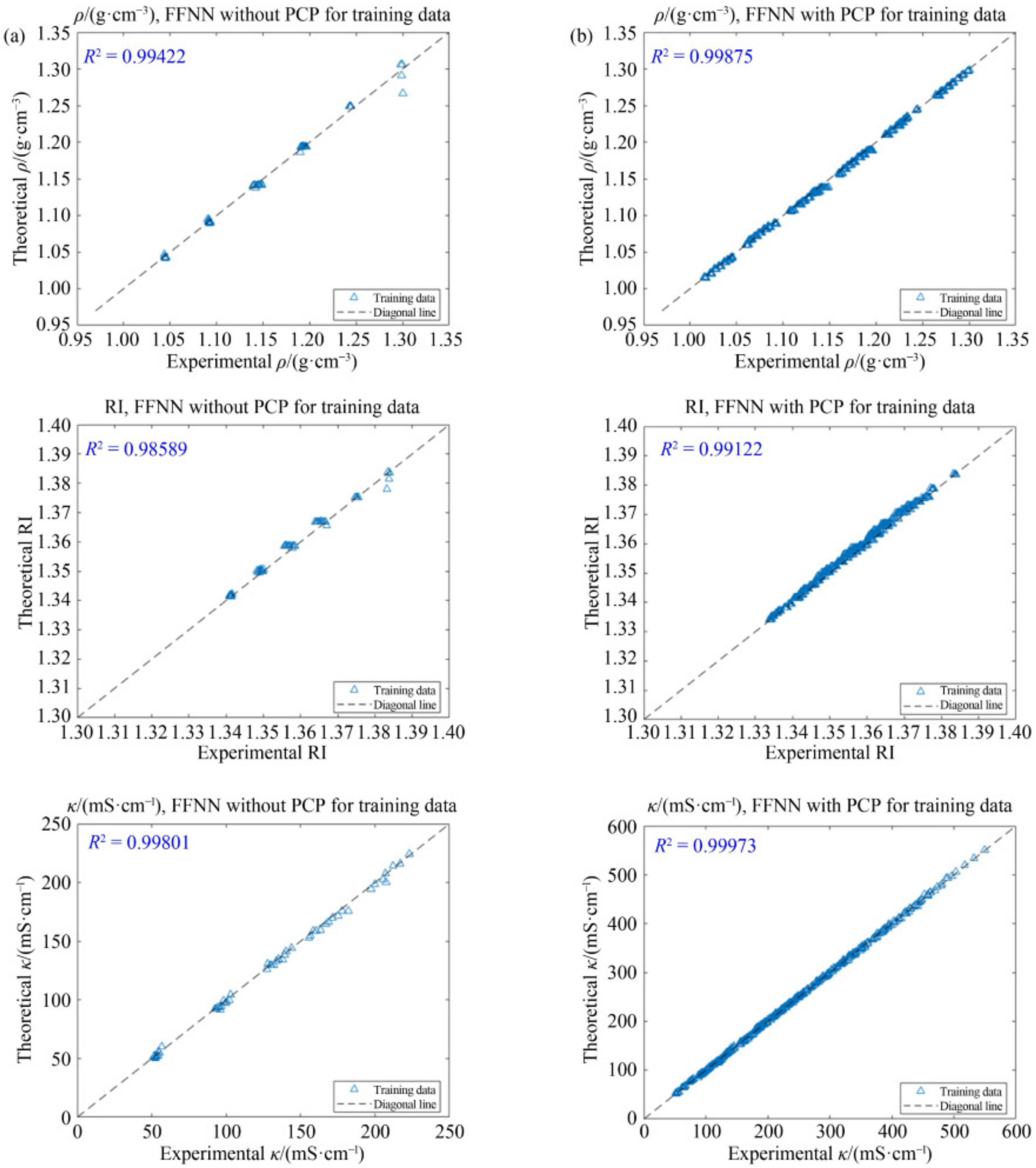

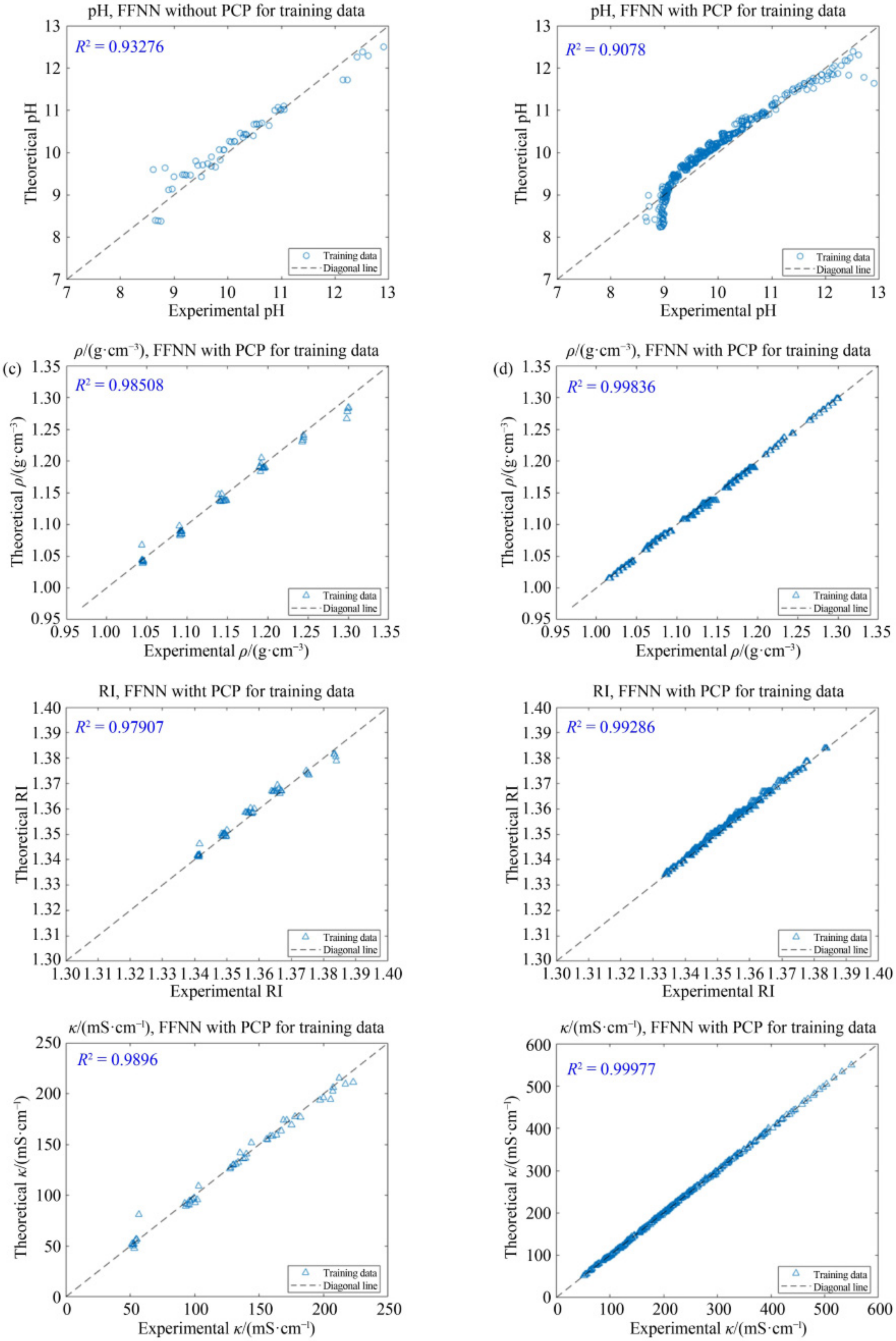
pH, FFNN without PCP for training data
R² = 0.93276
Theoretical pH
Experimental pH
Training data
Diagonal line
pH, FFNN with PCP for training data
R² = 0.9078
Theoretical pH
Experimental pH
Training data
Diagonal line
(c)
ρ/(g·cm⁻³), FFNN with PCP for training data
R² = 0.98508
Theoretical ρ/(g·cm⁻³)
Experimental ρ/(g·cm⁻³)
Training data
Diagonal line
(d)
ρ/(g·cm⁻³), FFNN with PCP for training data
R² = 0.99836
Theoretical ρ/(g·cm⁻³)
Experimental ρ/(g·cm⁻³)
Training data
Diagonal line
RI, FFNN witht PCP for training data
R² = 0.97907
Theoretical RI
Experimental RI
Training data
Diagonal line
RI, FFNN with PCP for training data
R² = 0.99286
Theoretical RI
Experimental RI
Training data
Diagonal line
κ/(mS·cm⁻¹), FFNN with PCP for training data
R² = 0.9896
Theoretical κ/(mS·cm⁻¹)
Experimental κ/(mS·cm⁻¹)
Training data
Diagonal line
κ/(mS·cm⁻¹), FFNN with PCP for training data
R² = 0.99977
Theoretical κ/(mS·cm⁻¹)
Experimental κ/(mS·cm⁻¹)
Training data
Diagonal line

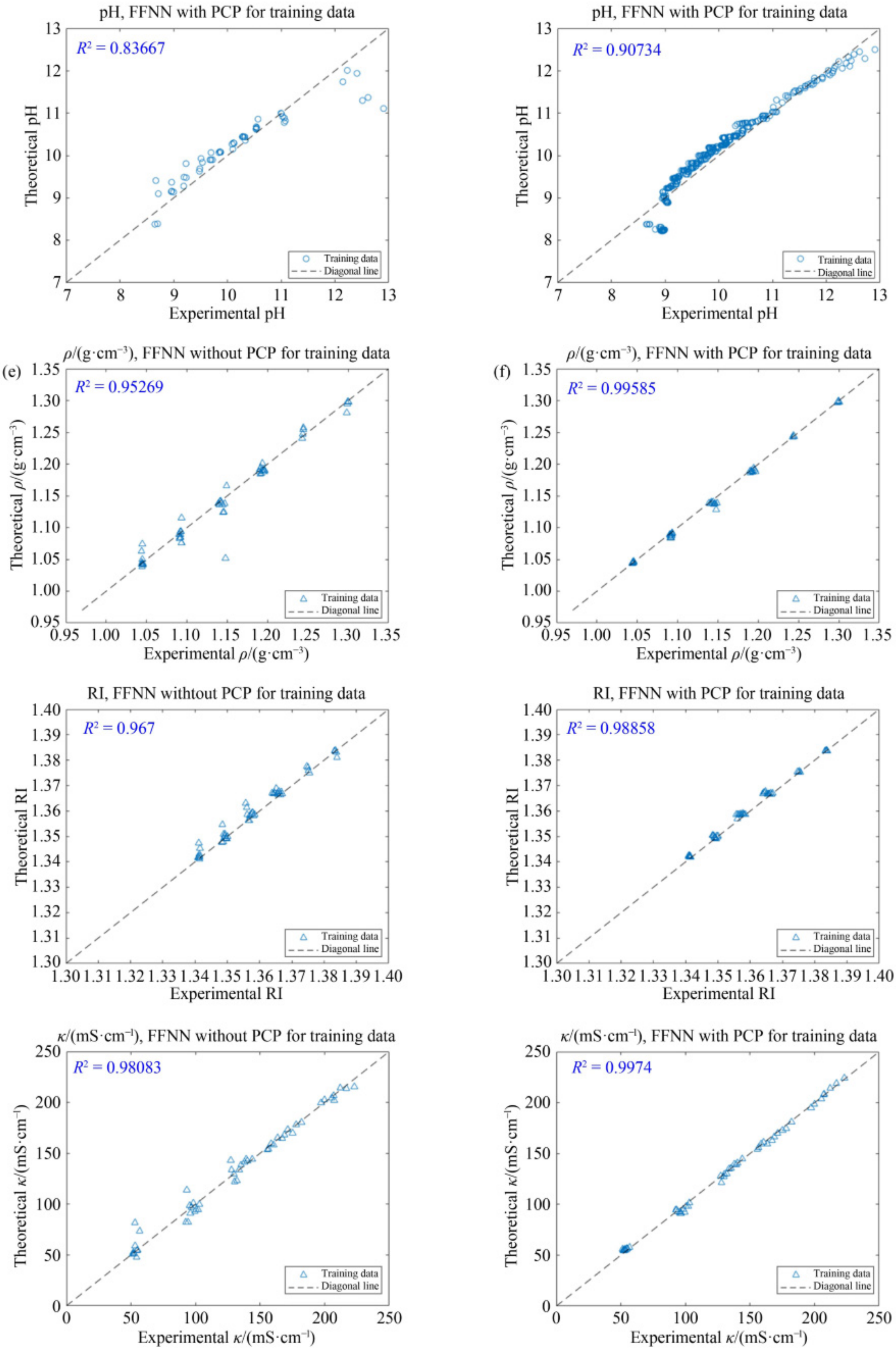

pH, FFNN with PCP for training data

pH, FFNN with PCP for training data

(e) ρ/(g·cm^{-3}), FFNN without PCP for training data

(f) ρ/(g·cm^{-3}), FFNN with PCP for training data

RI, FFNN withtout PCP for training data

RI, FFNN with PCP for training data

κ/(mS·cm^{-1}), FFNN without PCP for training data

κ/(mS·cm^{-1}), FFNN with PCP for training data

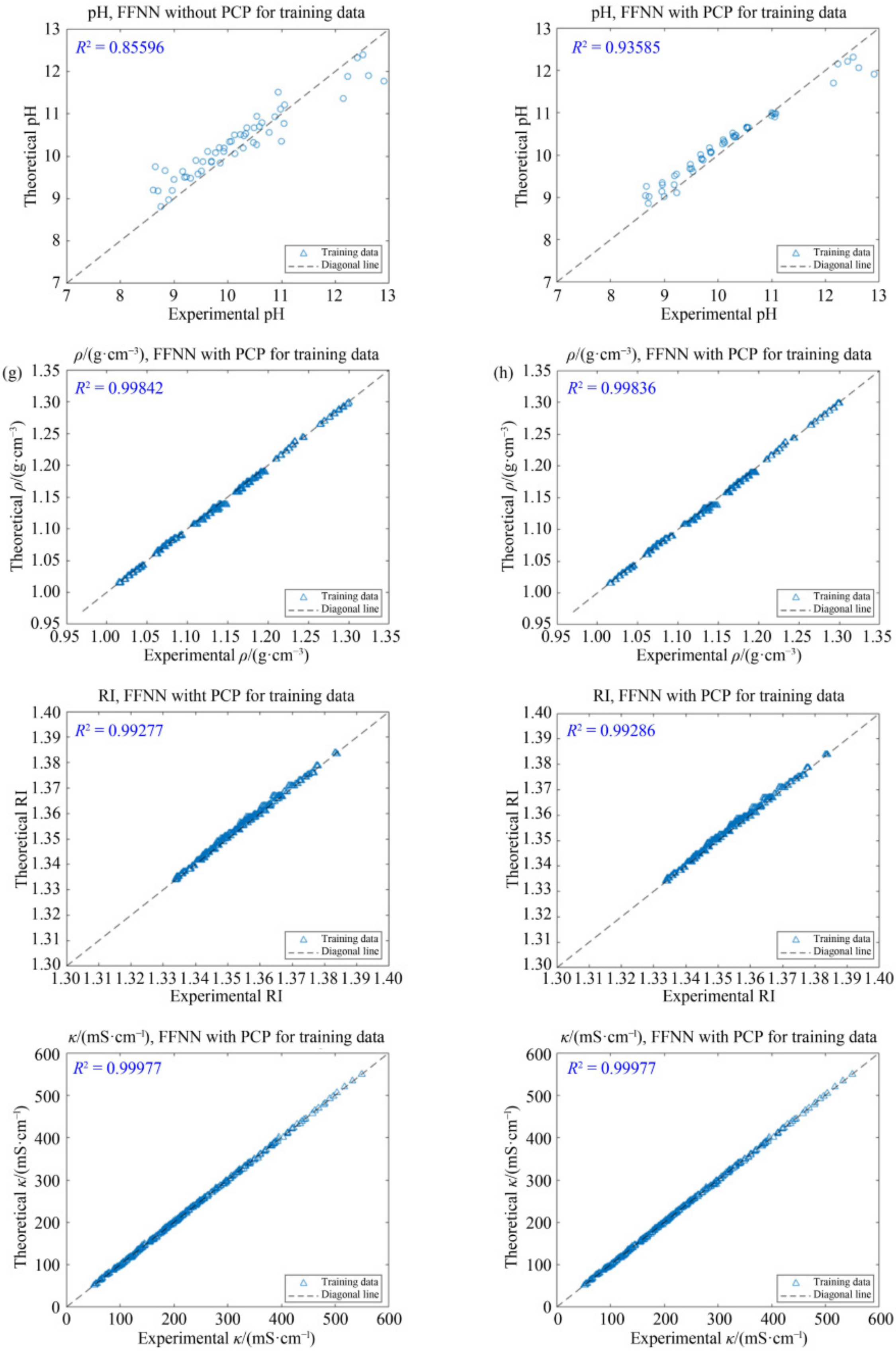
pH, FFNN without PCP for training data
$R^2 = 0.85596$
Theoretical pH
Experimental pH
Training data
Diagonal line
pH, FFNN with PCP for training data
$R^2 = 0.93585$
Theoretical pH
Experimental pH
Training data
Diagonal line
(g)
ρ/(g·cm^{-3}), FFNN with PCP for training data
$R^2 = 0.99842$
Theoretical ρ/(g·cm^{-3})
Experimental ρ/(g·cm^{-3})
Training data
Diagonal line
(h)
ρ/(g·cm^{-3}), FFNN with PCP for training data
$R^2 = 0.99836$
Theoretical ρ/(g·cm^{-3})
Experimental ρ/(g·cm^{-3})
Training data
Diagonal line
RI, FFNN witht PCP for training data
$R^2 = 0.99277$
Theoretical RI
Experimental RI
Training data
Diagonal line
RI, FFNN with PCP for training data
$R^2 = 0.99286$
Theoretical RI
Experimental RI
Training data
Diagonal line
κ/(mS·cm^{-1}), FFNN with PCP for training data
$R^2 = 0.99977$
Theoretical κ/(mS·cm^{-1})
Experimental κ/(mS·cm^{-1})
Training data
Diagonal line
κ/(mS·cm^{-1}), FFNN with PCP for training data
$R^2 = 0.99977$
Theoretical κ/(mS·cm^{-1})
Experimental κ/(mS·cm^{-1})
Training data
Diagonal line

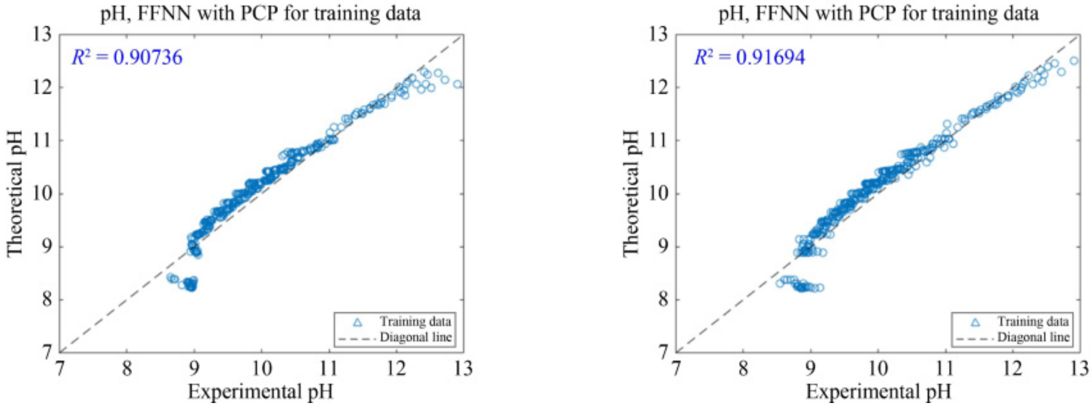

Fig. 9 Parity plots comparing the experimental and calculated PCPs based on predicted X and θ values from the trained FFNN model using proposed empirical and mechanistic equations: (a) FTIR, (b) PCP, (c) PCP and FTIR at $T = 20$ °C, (d) PCP and FTIR at various T values, (e) UV-Vis, (f) PCP and UV-Vis at $T = 20$ °C, (g) PCP and UV-Vis at various T values, and (h) FTIR, UV-Vis, and PCP excluding pH.

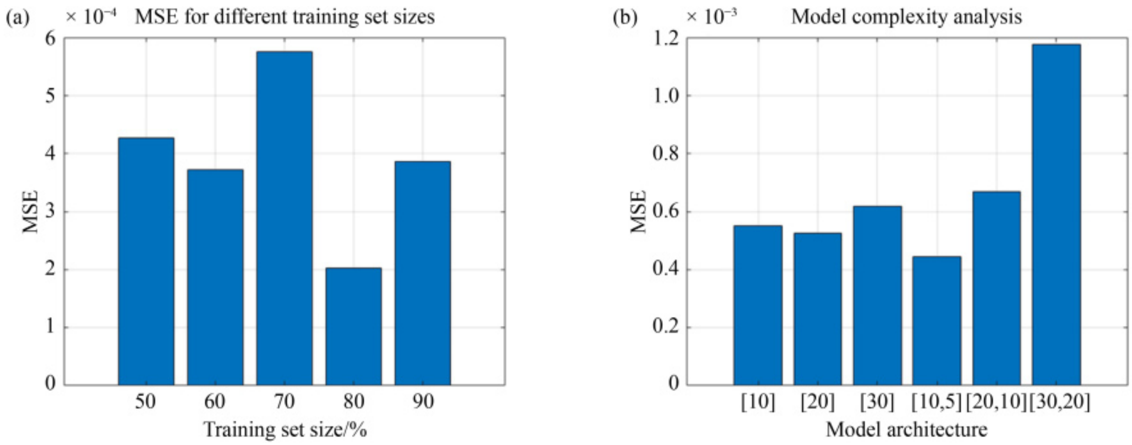

Fig. 10 MSE values obtained from the FFNN model for different (a) training set sizes, and (b) model architectures (highlighting the effect of varying the number of hidden layers and neurons per layer).

3.5.4 Model's robustness analysis

The robustness of the model was assessed using two methods: LOOCV and *k*-fold cross validation, and the results are presented here.

3.5.4.1 LOOCV method

The results of the robustness analysis using the LOOCV method indicate that the model demonstrates high reliability. The R^2 values obtained for the parity plots are 0.9969 for θ and 0.9999 for X, which reflect a strong correlation between the predicted and experimental values as demonstrated in Figs. 11(a) and 11(b). This suggests that the model is effectively capturing the underlying relationships in the data. Moreover, the normalized values for θ and X across different data subsets remain closely aligned with the zero-point line, indicating minimal scatter as is shown in Figs. 11(c) and 11(d). This consistency further reinforces the robustness of the model, as it shows that predictions are stable and reliable across various data conditions. Overall, these findings confirm that the model can be confidently utilized for predicting θ and X in diverse scenarios.

3.5.4.2 *k*-fold cross validation method

The results from the *k*-fold cross-validation demonstrate the robustness of the model, as evidenced by the normalized values for both θ and X in Figs. 11(e) and 11(f). In the generated plots, most of the normalized predictions cluster closely around the zero-point line, indicating that the model consistently produces results that are in line with the average predictions across all folds. Although some points exhibit slight discrepancies, these variations are minimal and do not detract from the overall accuracy of the model. This consistent performance across different subsets of the data highlights the model's ability to generalize well, reinforcing its reliability and robustness in predicting θ and X values across varying conditions as previously confirmed using the LOOCV method too. The observed

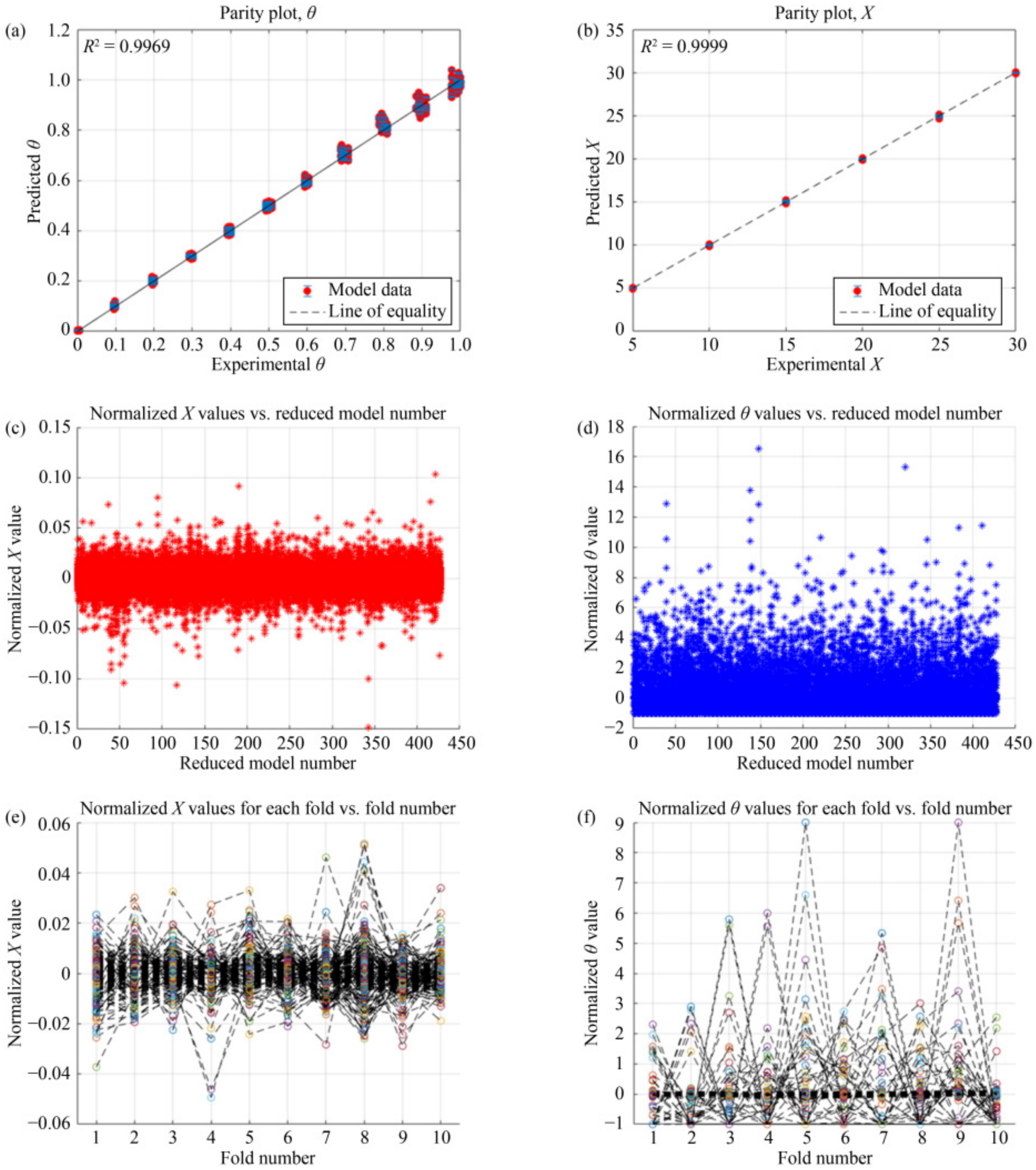

Fig. 11 Parity plots for (a) θ and (b) X for the model's robustness analysis using the LOOCV method, curves of normalized (c) θ and (d) X values across different data subsets for assessment of the model's robustness using the LOOCV method, and curves of normalized (e) θ and (f) X values across different fold numbers for assessment of the model's robustness using the k-fold cross validation method.

stability across folds suggests that the model is well-equipped to handle new, unseen data, further validating its effectiveness for practical applications.

4 Conclusions

The present study has successfully elucidated the relationships between key PCPs of K_2CO_3 solutions, namely ρ, RI, κ, and pH, as influenced by T, m, and θ. Through a systematic investigation, empirical models have been developed and validated, demonstrating a high degree of accuracy when compared with experimental data.

Our findings show that ρ increases with X and decreases with rising T. The model accurately reflects these variations. The RI increases with higher m and decreases with rising T, while θ has less influence. The model reliably captures these trends. κ increases with X and T, while it decreases with higher θ due to the shift from more mobile carbonate ions to less mobile bicarbonate ions. These trends are captured by the model. pH decreases with increasing θ and T. The model showed limitations due to its ideal solution assumptions, suggesting that future improvements should focus on refining reaction kinetics for real solutions.

The integration of a FFNN enabled highly accurate predictions of X and loading. Eight input scenarios were tested, with the best performance achieved using PCPs combined with FTIR or UV-Vis spectra at all T values. Acceptable results were also obtained using only PCPs. High R^2 values were achieved when substituting pH with FTIR and UV-Vis data, but predictions were less accurate using only FTIR or UV-Vis at 20 °C. Overall, combining physical and chemical property data with spectroscopic techniques significantly improved prediction accuracy, validating the model's effectiveness.

In conclusion, this research not only provides a comprehensive understanding of the PCPs of K_2CO_3 solutions but also establishes a framework for future studies. The findings hold significant implications for carbon capture technologies and related fields, as understanding the interactions within these solutions is crucial for optimizing processes aimed at mitigating CO_2 emissions. Continued exploration of these relationships will be vital as we strive for advancements in environmental technologies and sustainable practices.

Competing interests The authors declare that they have no competing interests.

Acknowledgements Financial support from the Swedish Energy Agency (Project number P2021-00008) is gratefully acknowledged.

Funding note Open Access funding enabled and organized by BIBSAM

References

1. Wang J, Azam W. Natural resource scarcity, fossil fuel energy consumption, and total greenhouse gas emissions in top emitting countries. Geoscience Frontiers, 2024, 15(2): 101757
2. Al-Mamoori A, Krishnamurthy A, Rownaghi A A, Rezaei F. Carbon capture and utilization update. Energy Technology, 2017, 5(6): 834–849
3. Yang Y, Xu W, Wang Y, Shen J, Wang Y, Geng Z, Wang Q, Zhu T. Progress of CCUS technology in the iron and steel industry and the suggestion of the integrated application schemes for China. Chemical Engineering Journal, 2022, 450: 138438
4. Chu H, Huang Z, Zhang Z, Yan X, Qiu B, Xu N. Integration of carbon emission reduction policies and technologies: research progress on carbon capture, utilization and storage technologies. Separation and Purification Technology, 2024, 343: 127153
5. Bui M, Adjiman C S, Bardow A, Anthony E J, Boston A, Brown S, Fennell P S, Fuss S, Galindo A, Hackett L A, et al. Carbon capture and storage (CCS): the way forward. Energy & Environmental Science, 2018, 11(5): 1062–1176
6. Ekemezie I O, Digitemie W N. Carbon capture and utilization (CCU): a review of emerging applications and challenges. Engineering Science and Technology Journal, 2024, 5(3): 949–961
7. Wilberforce T, Baroutaji A, Soudan B, Al-Alami A H, Olabi A G. Outlook of carbon capture technology and challenges. Science of the Total Environment, 2019, 657: 56–72
8. Tiwari T, Kaur G A, Singh P K, Balayan S, Mishra A, Tiwari A. Emerging bio-capture strategies for greenhouse gas reduction: navigating challenges towards carbon neutrality. Science of the Total Environment, 2024, 929: 172433
9. Makepa D C, Chihobo C H. Sustainable pathways for biomass production and utilization in carbon capture and storage—a review. Biomass Conversion and Biorefinery, 2024, 1–23
10. Fajardy M, Mac Dowell N. Can BECCS deliver sustainable and resource efficient negative emissions? Energy & Environmental Science, 2017, 10(6): 1389–1426
11. Chao C, Deng Y, Dewil R, Baeyens J, Fan X. Post-combustion carbon capture. Renewable & Sustainable Energy Reviews, 2021, 138: 110490
12. Yeung F D, Sammarchi S, Wang E, Gao Q, Li J. Interdisciplinary challenges in bio-energy carbon capture utilization & storage deployment: a review. Carbon Capture Science & Technology, 2024, 13: 100283
13. Bui M, Gunawan I, Verheyen V, Artanto Y, Meuleman E, Feron P. Dynamic modeling and validation of post-combustion CO_2 capture plants in Australian coal-fired power stations. Energy Procedia, 2013, 37: 2694–2702
14. Astuti A R A, Wenten I G, Ariono D, Sasongko D, Saputera W H, Khoiruddin K. Advances in carbon control technologies for flue gas cleaning. Separation and Purification Reviews, 2024, 53(4): 487–516
15. Lu G, Wang Z, Bhatti U H, Fan X. Recent progress in carbon dioxide capture technologies: a review. Clean Energy Science and Technology, 2023, 1(1): 32
16. Amann J M G, Bouallou C. A new aqueous solvent based on a blend of N-methyldiethanolamine and triethylene tetramine for CO_2 recovery in post-combustion: kinetics study. Energy Procedia, 2009, 1(1): 901–908
17. Patiño-Echeverri D, Hoppock D C. Reducing the energy penalty costs of postcombustion CCS systems with amine-storage. Environmental Science & Technology, 2012, 46(2): 1243–1252
18. Bahman N, Al-Khalifa M, Al Baharna S, Abdulmohsen Z, Khan

E. Review of carbon capture and storage technologies in selected industries: potentials and challenges. Reviews in Environmental Science and Biotechnology, 2023, 22(2): 451–470

19. Sultan H, Quach T Q, Muhammad H A, Bhatti U H, Lee Y D, Hong M G, Baek I H, Chan N S. Advanced post combustion CO_2 capture process—a systematic approach to minimize thermal energy requirement. Applied Thermal Engineering, 2021, 184: 116285
20. Strojny M, Gładysz P, Hanak D P, Nowak W. Comparative analysis of CO_2 capture technologies using amine absorption and calcium looping integrated with natural gas combined cycle power plant. Energy, 2023, 284: 128599
21. Yagmur Goren A, Erdemir D, Dincer I. Comprehensive review and assessment of carbon capturing methods and technologies: an environmental research. Environmental Research, 2024, 240: 117503
22. Wu H, Zhang X, Wu Q. Research progress of carbon capture technology based on alcohol amine solution. Separation and Purification Technology, 2024, 333: 125715
23. He X, He H, Barzagli F, Amer M W, Li C, Zhang R. Analysis of the energy consumption in solvent regeneration processes using binary amine blends for CO_2 capture. Energy, 2023, 270: 126903
24. Matin N S, Remias J E, Neathery J K, Liu K. Facile method for determination of amine speciation in CO_2 capture solutions. Industrial & Engineering Chemistry Research, 2012, 51(19): 6613–6618
25. Vasiliu D, Yazdani A, McCann N, Irfan M, Schneider R, Rolker J, Maurer G, von Harbou E, Hasse H. Thermodynamic study of a complex system for carbon capture: butyltriacetonediamine plus water plus carbon dioxide. Journal of Chemical & Engineering Data, 2016, 61(11): 3814–3826
26. Kejla L, Svoboda P, Sedlácek J, Simácek P. Gravimetric titrations in a modern analytical laboratory: evaluation of performance and practicality in everyday use. Chemicke Zvesti, 2022, 76(4): 2051–2058
27. Karamé I, Shaya J, Srour H. Process Analytical Technology for CO_2 Capture. 1st ed. London: IntechOpen, 2018, 185–210
28. Smith K, Xiao G, Mumford K, Gouw J, Indrawan I, Thanumurthy N, Quyn D, Cuthbertson R, Rayer A, Nicholas N, et al. Demonstration of a concentrated potassium carbonate process for CO_2 capture. Energy & Fuels, 2014, 28(1): 299–306
29. Hu G, Nicholas N J, Smith K H, Mumford K A, Kentish S E, Stevens G W. Carbon dioxide absorption into promoted potassium carbonate solutions: a review. International Journal of Greenhouse Gas Control, 2016, 53: 28–40
30. Ameri A. Density, refractive index, electrical conductivity, pH, FTIR and UV-Vis spectra of potassium carbonate-potassium bicarbonate-water system. Journal of Chemical & Engineering Data, 2025, 70(2): 766–786
31. Li C X, Park S B, Kim J S, Lee H. A new generalized model for predicting the density of single- and mixed-electrolyte solutions. Fluid Phase Equilibria, 1998, 145(1): 1–14
32. Li C, Lee H. Density calculation of electrolyte solutions with the solution osmotic pressure. Chemical Engineering Science, 2000, 55(3): 655–665
33. Laliberté M, Cooper W E. Model for calculating the density of aqueous electrolyte solutions. Journal of Chemical & Engineering Data, 2004, 49(5): 1141–1151
34. Lam E J, Alvarez M N, Galvez M E, Alvarez E B. A model for calculating the density of aqueous multicomponent electrolyte solutions. Journal of the Chilean Chemical Society, 2008, 53(1): 1393–1398
35. Tang I N, Munkelwitz H R. Simultaneous determination of refractive index and density of an evaporating aqueous solution droplet. Aerosol Science and Technology, 1991, 15(3): 201–207
36. Leyendekkers J V, Hunter R J. Refractive index of aqueous electrolyte solutions. Extrapolations to other temperatures, pressures, and wavelengths and to multicomponent systems. Journal of Chemical & Engineering Data, 1977, 22(4): 427–431
37. Leyendekkers J V, Hunter R J. The Tammann-Tait-Gibson model for aqueous electrolyte solutions. Application to the refractive index. Journal of Physical Chemistry, 1977, 81(17): 1657–1663
38. Alavia W, Soto I, Lovera J A. Modeling of the refractive index for the systems MX + H_2O, M_2X + H_2O, H_3BO_3 + MX + H_2O, and H_3BO_3 + M_2X + H_2O. Processes, 2021, 9(3): 525
39. Farooque U, Singh S K, Rashid T, Alam M I. Simple model for the calculation of concentration and temperature dependent refractive index of different solutions. Turkish Computational and Theoretical Chemistry, 2023, 7(3): 17–23
40. Bernard O, Kunz W, Turq P, Blum L. Conductance in electrolyte solutions using the mean spherical approximation. Journal of Physical Chemistry, 1992, 96(9): 3833–3840
41. de Diego A, Madariaga J M, Chapela E. Empirical model of general application to fit (*k, c, T*) experimental data from concentrated aqueous electrolyte solutions. Electrochimica Acta, 1997, 42(9): 1449–1456
42. de Diego A, Usobiaga A, Madariaga J M. Modification of the Falkenhagen equation to fit conductimetric data for concentrated electrolyte solutions. Journal of Electroanalytical Chemistry, 1997, 430(1-2): 263–268
43. Chandra A, Bagchi B. Ion conductance in electrolyte solutions. Journal of Chemical Physics, 1999, 110(20): 10024–10034
44. Wang P, Anderko A, Young R D. Modeling electrical conductivity in concentrated and mixed-solvent electrolyte solutions. Industrial & Engineering Chemistry Research, 2004, 43(25): 8083–8092
45. Ding M S. Casteel-Amis equation: its extension from univariate to multivariate and its use as a two-parameter function. Journal of Chemical & Engineering Data, 2004, 49(5): 1469–1474
46. Ding M S, von Cresce A, Xu K. Conductivity, viscosity, and their correlation of a super-concentrated aqueous electrolyte. Journal of Physical Chemistry C, 2017, 121(4): 2149–2153
47. Bernard O, Aupiais J. Conductivity of weak electrolytes for buffer solutions: modeling within the mean spherical approximation. Journal of Molecular Liquids, 2018, 272: 631–637
48. Zhang W, Chen X, Wang Y, Wu L, Hu Y. Experimental and modeling of conductivity for electrolyte solution systems. ACS Omega, 2020, 5(35): 22465–22474
49. Boroujeni S N, Liang X, Maribo-Mogensen B, Kontogeorgis G M. Comparison of models for the prediction of the electrical conductivity of electrolyte solutions. Industrial & Engineering

Chemistry Research, 2022, 61(8): 3168–3185

50. Kell G S. Density, thermal expansivity, and compressibility of liquid water from 0 to 150 °C: correlations and tables for atmospheric pressure and saturation reviewed and expressed on 1968 temperature scale. Journal of Chemical & Engineering Data, 1975, 20(1): 97–105
51. Schiebener P, Straub J, Levelt Sengers J M H, Gallagher J S. Refractive index of water and steam as function of wavelength, temperature and density. Journal of Physical and Chemical Reference Data, 1990, 19(3): 677–717
52. Danckwerts P V, Sharma M M. The absorption of carbon dioxide into solutions of alkalis and amines (with some notes on hydrogen sulfide and carbonyl sulfide). Chemical Engineering, 1966, 44(3): 244–256